Electronic Supplementary Material (ESI) for Energy & Environmental Science.

Supporting Information

Defect-rich and ultrathin N doped carbon nanosheets as advanced trifunctional metal-free electrocatalysts for ORR, OER and HER

Hao Jiang,[ab] Jinxing Gu,[c] Xusheng Zheng,[d] Min Liu,[e] Xiaoqing Qiu,[a] Liangbing Wang,[f] Wenzhang Li,[ag*] Zhongfang Chen,[c*] Xiaobo Ji,[a] Jie Li[ag*]

[a] School of Chemistry and Chemical Engineering, Central South University, Changsha, 410083, China

[b] College of Materials and Chemical Engineering, Hunan City University, Yiyang, 413000, China

[c] Department of Chemistry, University of Puerto Rico Rio Piedras Campus, San Juan, PR 00931, USA

[d] Hefei National Laboratory for Physical Sciences at the Microscale, National Synchrotron Radiation Laboratory, University of Science and Technology of China, Hefei, Anhui, 230026, China

[e] Institute of Super-microstructure and Ultrafast Process in Advanced Materials, School of Physics and Electronics, Central South University, Changsha, Hunan, China

[f] School of materials science and engineering, Central South University, Changsha, Hunan, China

[g] Hunan Provincial Key Laboratory of Chemical Power Sources, Central South University, Changsha 410083, Hunan, China.

*Corresponding author. Tel./fax: +86-731-88879616.

E-mail address: liwenzhang@csu.edu.cn (WL), zhongfangchen@gmail.com (ZC), lijieliu@csu.edu.cn (JL)

Experimental Section

1 Sample preparation

Preparation of ultrathin nitrogen doped carbon nanosheets (NCNs)

In a typical synthesis, 5 g of citric acid (Alfa Aesar, AR) and 5 g of NH_4Cl (Alfa Aesar, AR) were added into 15 mL of deionized water (18.2 MΩ cm) to form a homogeneous and transparent solution under ultrasonication followed by violently stirring for 1 h at room temperature (25 ^{o}C). Subsequently, the homogeneous solution was heated to evaporate solvent and dried at 60 ^{o}C for 12 h to form solid mixtures. A well-mixed reactant powder was obtained after grounding the solid mixtures about 10 min. The precursor powder was then carbonized at different temperatures (800, 900 and 1000 °C) for 3 h under Ar atmosphere at a heating rate of 10 ^{o}C min^{-1}. Finally, the black products with fluffy structure were obtained, which were named as NCN-800-5, NCN-900-5 and NCN-1000-5 (the number of 5 represents the mass of NH_4Cl in precursor is 5 g), respectively.

Preparation of nitrogen doped carbon nanosheets (NCNs) with different mass of NH_4Cl.

To investigate the effect of NH_4Cl on the structure and electrocatalytic performance of the NCNs, the NCN-1000-2.5 and NCN-1000-1 were prepared by the same process as NCN-1000-5 sample, but with different ratios of citric acid to NH_4Cl. Namely, 2.5 and 1 g NH_4Cl were used in the precursors to prepare NCN-1000-2.5 and NCN-1000-1.

Preparation of undoped porous carbon (C-1000).

For comparison, the undoped carbon was also synthesized by the carbonization of citric acid alone at 1000 °C with other conditions unchanged, which was defined as C-1000.

2 Materials characterization

X-ray diffraction (XRD) patterns were obtained from an X-ray diffractometer (SIMENS d500) with Cu Kα radiation (λ=1.5406 Å) to investigate the crystal structure of each sample. The surface morphologies of products were analyzed by the scanning electron microscope (SEM, Nova NanoSEM 230). The detailed microstructure of samples was analyzed by a transmission electron microscope (TEM, FEI TECNAI G2 F20). Atomic force microscopy (AFM, Bruker, ICON2-SYS) was utilized to measure the thickness information of NCN samples. N_2 adsorption/desorption tests were conducted at 77 K by a gas adsorption analyzer (JW-BK132F, Beijing). The specific surface area and pore size of the samples were calculated by Brunauere-Emmette-Teller (BET) and Barrett-Joyner-Halenda (BJH) models, respectively. Raman spectra of the samples were obtained from a LabRAM Hr800 confocal Raman microscopic system under an excitation laser of 532 nm. A X-ray photoelectron spectroscopy (XPS) spectrometer (K-Alpha 1063) was used to detect the surface elemental composition and bonding configuration of the as-prepared samples. Fourier transform infrared spectrophotometer (FTIR, AVTA-TAR, 370) was used to detect the functional groups on the surface of the as-prepared samples over a range of 400 to 4,000 cm^{-1} with a resolution of 2 cm^{-1}. The content of transition metals (Fe, Co and Ni) in NCNs was detected by the inductively coupled plasma emission spectrometer (ICP-AES, Shimadzu). The NCNs sample was firstly soaked and digested in HNO_3 solution (3 M) for 24 h, and then analyzed by ICP-AES instrument. The C and N K-edge NEXAFS spectra were measured at the photoemission end-station at beamline BL10B in the National Synchrotron Radiation Laboratory (NSRL) in Hefei, China. A bending magnet is connected to the beamline, which is equipped with three gratings covering photon energies from 100 to 1000 eV. In this experiment, the samples were kept in the total electron yield mode under an ultrahigh vacuum at 5×10^{-10} mbar. The resolving power of the grating was typically $E/\triangle E = 1000$, and the photon flux was 1×10^{-10} photons per s. The NEXAFS raw data were normalized to the photoelectron current of the photon beam, measured on an Au wafer.

3 Electrochemical measurements

Electrode preparations

The rotating disk electrode (RDE, 0.196 cm^2) was polished with alumina slurry and rinsed with distilled water before the catalyst was loaded on the disk. The catalyst ink was prepared by dispersing 4 mg catalytic powders into 10 μL Nafion (5 wt.%) and 990 μL ethanol (98 vol.%) mixed solution. Subsequently, the mixed solution was sonicated for several ten-minutes to form homogeneous catalytic ink. Finally, 10 μL of catalyst ink was placed on the glassy carbon RDE. After dried at ambient temperature, the catalyst with a content of 0.2 mg cm^{-2} was loaded on the working electrode. As comparison, commercial Pt/C (20 wt.%) and RuO_2 (Alfa Aesar, 99.95%) catalyst inks were also prepared with the same method.

Testing Conditions

The ORR, OER and HER activities of the as-prepared catalysts were tested on Zahner (Zennium, Germany) electrochemical analyzer attached with a Pine rotating disk electrode (RDE) system (Pine Instruments Co. Ltd. USA). All of the electrochemical measurements were performed in a normal three-electrode system. A graphite rod (Alfa Aesar, 99.9995%) was used as the counter electrode for HER while a Pt foil (0.25 cm^2) was used as the counter electrode for ORR and OER tests, respectively. A KCl-saturated Ag/AgCl electrode was used as the reference electrode. 0.1 M KOH and 0.5 M H_2SO_4 aqueous solution were respectively served as electrolyte in the process of electrochemical measurements and deaerated by high purity O_2 and N_2 (99.99% pure) according to the concrete conditions. All the potentials in this work were converted to a reversible hydrogen electrode (RHE), E(RHE)=E(Ag/AgCl) + 0.198 V + 0.059×pH.

ORR tests

The ORR performance of the as-prepared samples was first investigated by cyclic voltammetry (CV) in N_2/O_2-saturated 0.1 M KOH and 0.5 M H_2SO_4 at room temperature, with a sweep rate of 50 mV s^{-1}. Linear sweep voltammetry (LSV) experiments were conducted under constant O_2 gas flow at 5 mV s^{-1} under rotating speeds varying from 400 to 1600 rpm. The ORR onset potential (E_{onset}) is defined as the potential at the intersection of the tangents just before and after the onset of rise in the disc current in the RDE LSV curve. The K-L equations (S1-S3) are used to calculate the kinetic current density (J_k) and transferred electron numbers (n):

$$\frac{1}{J}=\frac{1}{J_k}+\frac{1}{B\omega^{1/2}} \tag{S1}$$

$$B=0.2nFD_0^{2/3}\nu^{-1/6}C_0 \tag{S2}$$

$$J_k=nFkC_0 \tag{S3}$$

where J and J_k are the measured current density and the kinetic current density, respectively. ω is the electrode rotation speed, F is the Faraday constant (96485 C mol^{-1}), D_0 is the diffusion coefficient of O_2 (1.9×10^{-5} cm^2 s^{-1} for 0.1 M KOH and 1.15×10^{-5} cm^2 s^{-1} for 0.5 M H_2SO_4), ν is the kinetic viscosity (0.01 cm^2 s^{-1}), and C_0 is the concentration of O_2 (1.2×10^{-6} mol cm^{-3}).

The stability of samples was tested by the current-time (*i-t*) chronoamperometric responses at 0.67 and 0.4 V (vs. RHE) in 0.1 M KOH and 0.5 M H_2SO_4 for 12000 s, respectively. Methanol tolerance test was implemented through *i-t* response at the above potentials with 0.5 mL methanol (3 M) addition at 300 s.

OER tests

The OER performance of the as-prepared samples was also investigated by LSV experiments with a scan rate of 5 mV s^{-1} in O_2 saturated 0.1 M KOH. The potentials were iR_s (i = catalytic current and R_s = solution resistance) corrected using the E-iR_s relation. The value of R_s is determined by the high-frequency intercept from the Nyquist plot obtained by the electrochemical impedance spectroscopy (EIS) technique. The overall oxygen electrode activity can be estimated by ΔE and defined as follows:

$$\Delta E=E_{OER@j=10}-E_{ORR@j=3} \tag{S4}$$

where $E_{OER@j=10}$ is the potential at 10 mA cm^{-2} for OER and $E_{ORR@j=3}$ is the potential at 3 mA cm^{-2} for ORR.

Electrochemical impedance spectroscopy (EIS) tests were implemented on Zahner (Zennium, Germany) electrochemical analyzer in the frequency range of 100 KHz to 10 mHz. The applied potential and excitation amplitude were set as 1.6 V (vs. RHE) and 5 mV, respectively.

The OER stability of samples was tested by the *i-t* chronoamperometric responses at 1.5 V (vs. RHE) for 12000 s and LSV experiments before and after 500 extensive cycles in 0.1 M KOH.

HER tests

The HER performance of the as-prepared samples was also investigated by LSV experiments with a scan rate of 5 mV s^{-1} in N_2 saturated 0.5 M H_2SO_4 electrolyte. The long-term stability of NCN-1000-5 was tested by the *i-t* chronoamperometric responses at -0.15 V (vs. RHE) for 12000 s and LSV experiments before and after 500 extensive cycles in 0.5 M H_2SO_4.

4 Zn-air battery assembly and measurement

To evaluate the performance of Zn-air batteries, a home-made battery was constructed. The air electrode for Zn-air battery contained three layers (Figure S27): catalytic layer (CL), nickel foam (0.1 mm) and gas diffusion layer (GDL). The CL was fabricated by catalysts (NCN-1000-5), ketjen black (ECP-600JD) and acetylene black, as conductive additive, polytetrafluoroethylene emulsion (PTFE, 60 wt %), as binder, were mixed uniformly in a weight ratio of 3:3:1:3. The GDL was fabricated by rolling press the acetylene black, ammonium oxalate and PTFE hybrid slurry (mass ratio: 2:1:7), which were dispersed in ethanol. The total thickness of the air electrode was 0.4 to 0.6 mm after pressed at 10 MPa. Then, the air electrode was dried at 200 ^{o}C for 1 h in a vacuum oven. Finally, the Zn-air batteries were assembled with a polished Zn plate (thickness: 0.3 mm, purity: 99.99 wt.%) as the anode, 6 M KOH and 0.2 M $Zn(Ac)_2$ as the electrolyte and the prepared CL (an effective geometric area of 1 cm^2, catalyst loading amount of 2.0 mg cm^{-2}) as cathode in a home-made cell model. For comparison, the rechargeable battery was also made from a mixture of commercial Pt/C (20 %) and RuO_2 (99.95 %) with a mass ratio of 1:1.

All battery testing measurements were operated under ambient atmosphere. The polarization curves (V-i) were obtained by LSV technique (5 mV s^{-1}) with Zahner electrochemical working station. The galvanostatic discharge and charge cycling (10 min discharge and 10 min charge with the current density of 10 mA cm^{-2}) were performed in LAND CT2001C testing system. The red light-emitting diodes (LED, 2V) is commercial available. Both the current density and power density were normalized to the effective surface area of air electrode. The specific capacity was calculated according the equation S5:

$$\frac{current\ *\ discharge\ time}{weight\ of\ consumed\ zinc}$$

(S5)

The energy density was calculated according the equation S6:

$$\frac{current\ *\ discharge\ time\ *average\ discharge\ voltage}{weight\ of\ consumed\ zinc}$$

(S6)

5 Computational Studies

Computational method

Our spin-polarized density functional theory (DFT) computations were performed using the $Dmol^3$ code utilizing the PBE functional and double numerical plus polarization (DNP) basis set.[1-3] To simulate the reactions in the H_2O solvent environment, the conductor-like screen model (COSMO) with the dielectric constant of 78.54 was applied. The van der Waals interactions were described using the empirical correction in Grimme scheme.[4] Self-consistent field (SCF) calculations were performed with a convergence criterion 10^{-6} a.u. The Monkhorst-Pack method was utilized to generate *k* points to sample the Brillouin zone, and the *k*-points grids are $2 \times 3 \times 1$ and $1 \times 3 \times 1$ for N-doped graphene sheets and nanoribbons, respectively.

ORR and OER

The overpotential of the ORR/OER can be determined by examining the reaction Gibbs free energies of the different mechanistic steps. The thermochemistry of these electrochemical reactions was obtained by DFT computations in conjunction with the computational hydrogen electrode (CHE) model developed by Nørskov *et al.*[5, 6] ORR can proceed either through a two-step $2e^-$ pathway that reduces O_2 to H_2O_2, or completely via a direct $4e^-$ process in which O_2 is reduced directly to H_2O. Our electrochemical test results have confirmed that a $4e^-$ pathway proceeds on the N doped carbon materials. Hereby, the $4e^-$ reaction mechanism for ORR in acidic condition could be written as [7]:

$$O_2(g) + H^+ + e^- + * = *OOH \quad \text{(S7a)}$$

$$*OOH + H^+ + e^- = *O + H_2O(l) \quad \text{(S7b)}$$

$$*O + H^+ + e^- = *OH \quad \text{(S7c)}$$

$$*OH + H^+ + e^- = * + H_2O(l) \quad \text{(S7d)}$$

where * represents the active site on the surface of simulated carbon structures, g and l refer to the gas and liquid phase, respectively, and *OOH, *OH and *O denote the adsorbed intermediates. As a reverse reaction of ORR, the mechanism for OER could be written as:

$$H_2O(l) + * = *OH + H^+ + e^- \quad \text{(S8a)}$$

$$*OH = *O + H^+ + e^- \quad \text{(S8b)}$$

$$*O + H_2O(l) = *OOH + H^+ + e^- \quad \text{(S8c)}$$

$$*OOH = O_2(g) + H^+ + e^- + * \quad \text{(S8d)}$$

The Gibbs free adsorption energy (ΔG) is used as a descriptor to represent the interaction between adsorbates and active sites.[6] For instance,

$$2H_2O + * = *OOH + 3/2(H^+ + e^-) \quad \text{(S9a)}$$

$$\Delta G(*OOH) = G(*OOH) + 3/2G(H_2) - 2G(H_2O) - G(*) \quad \text{(S9b)}$$

The free energy of each species can be calculated by the following equation:

$$G = E + E_{ZPE} - TS \quad \text{(S10)}$$

where T denotes the temperature of 298.15 K, and S represents the entropy. The zero-point energy (E_{ZPE}) and entropy (S) of H_2 gas molecule and H_2O gas molecule are from the handbook.[8] The computational hydrogen electrode (CHE) model can be written as $H^+ + e^- = 1/2H_2$, so that at 298.15 K, 100 kPa, and pH = 0, the free energy of ($H^+ + e^-$) is $1/2G(H_2)$. The thermodynamic data of gas H_2O is under the pressure of 0.035 bar, at which the gas H_2O is in the phase equilibrium to the liquid H_2O. The free energy of O_2 gas is derived as $G(O_2) = 2G(H_2O) – 2G(H_2) + 4.92$ eV, since the DFT methods can not accurately calculate the energy of triplet O_2 molecule. The zero–point energies and entropies of adsorbates (*OOH, *OH and *O) are computed from the vibrational frequencies, in which only the adsorbate vibrational modes are calculated explicitly, while the catalyst was fixed.

We calculated ΔG(*OOH), ΔG(*O) and ΔG(*OH) of various probable active sites, as summarized in Table S13. They are used to compute the Gibbs free energy change for each mechanistic step of ORR/OER at different applied electrode potentials.[9] For example:

$$\Delta G(\text{S7a}) = \Delta G(\text{*OOH}) – 4.92 \text{ eV} + \text{eU}_1 \quad \text{(S11a)}$$

$$\Delta \text{G}(\text{S7b}) = \Delta \text{G}(\text{*O}) – \Delta \text{G}(\text{*OOH}) + \text{eU}_2 \quad \text{(S11b)}$$

$$\Delta \text{G}(\text{S7c}) = \Delta \text{G}(\text{*OH}) – \Delta \text{G}(\text{*O}) + \text{eU}_3 \quad \text{(S11c)}$$

$$\Delta \text{G}(\text{S7d}) = -\Delta \text{G}(\text{*OH}) + \text{eU}_4 \quad \text{(S11d)}$$

where U_i are the applied potential in the electrode. Since OER is a reverse reaction of ORR, we have ΔG(S8a) = -ΔG(S7d), ΔG(S8b) = -ΔG(S7c), ΔG(S8c) = -ΔG(S7b), and ΔG(S8d) = -ΔG(S7a).

As found by Nørskov and coworkers, ΔG(*OOH), ΔG(*O) and ΔG(*OH) are strongly correlated on metal surfaces,[10, 11] e.g. the following general relationships on (111) surfaces [12] :

$$\Delta G(\text{*OH}) = 0.5 \times \Delta G(\text{*O}) + \text{K}_{\text{OH}} \quad \text{(S12a)}$$

$$\Delta G(\text{*OOH}) = 0.5 \times \Delta G(\text{*O}) + K_{OOH} \tag{S12b}$$

Similar scaling relationships have been revealed on many catalytic processes, such as OER on oxide surfaces and ORR on Fe/N doped graphene.[5, 9] Thus, we explored the scaling relationships of ORR and OER on N-doped carbon nanosheets in Figure S24a, resulting in the following linear relationship:

$$\Delta G(\text{*OOH}) = 0.38 \times \Delta G(\text{*O}) + 3.45 \tag{S12c}$$

$$\Delta G(\text{*OH}) = 0.50 \times \Delta G(\text{*O}) + 0.22 \tag{S12d}$$

The slope of equation S12d is about 0.5, because unlike O radical adsorbed on the surface, OH and OOH radicals are absorbed on the electrocatalyst through single bonds. With our explored scaling relationship, ΔG(S7) can be derived as:

$$\Delta G(\text{S7a}) = 0.38\ \Delta G(\text{*O}) - 1.47 + eU_1 \tag{S13a}$$

$$\Delta G(\text{S7b}) = 0.62\ \Delta G(\text{*O}) - 3.45 + eU_2 \tag{S13b}$$

$$\Delta G(\text{S7c}) = -0.50\ \Delta G(\text{*O}) + 0.22 + eU_3 \tag{S13c}$$

$$\Delta G(\text{S7d}) = -0.50\ \Delta G(\text{*O}) - 0.22 + eU_4 \tag{S13d}$$

based on the ΔG(*O). When the Gibbs free energy change of a mechanistic step is 0, the corresponding potential is denoted as the reversible potential, U_i^0(i=1,2,3,4). The term U_i^0, can be derived as:

$$eU_1^0 = 1.47 - 0.38\ \Delta G(\text{*O}) \tag{S14a}$$

$$eU_2^0 = 3.45 - 0.62\ \Delta G(\text{*O}) \tag{S14b}$$

$$eU_3^0 = 0.50\ \Delta G(\text{*O}) - 0.22 \tag{S14c}$$

$$eU_4^0 = 0.50\ \Delta G(\text{*O}) + 0.22 \tag{S14d}$$

U_i^0 is related to the potential determining step (PDS), which determines the lower bound of the overpotential of ORR/OER. The reversible potentials of each selected active sites are summarized in Figure S24b, as well as the potential determining step (PDS), since the PDS for ORR/OER is the mechanistic step that has the smallest/largest reversible potential.

The overpotential (η) for ORR/OER can be determined as [5]:

$$\eta_{min}^{ORR} = 1.23 \text{ V} - \min(U_i^0) \tag{S15a}$$

$$\eta_{min}^{OER} = \max(U_i^0) - 1.23 \text{ V} \tag{S15b}$$

where U_i^0 (i=1,2,3,4) are the reversible potential of reactions (S8a) to (S8d) when ΔG(S7) = 0. A smaller η value indicates that the ORR/OER process on the surface of N-doped carbon nanosheets is more favorable. Within the scaling relationship and the overpotentials, we can derive the volcano plot as η versus the descriptor ΔG(*O) (Figure 9a).

HER

The Gibbs free energy of hydrogen absorbed to the active site forming *H intermediate is generally defined as the descriptor to evaluate the activity of HER electrocatalysts.[13] To evaluate the catalyst activity at different hydrogen coverage, we computed the differential Gibbs free energy for hydrogen adsorption, $\Delta G(*H_n)$. For the n_{th} H atom adsorbed to the active site, $\Delta G(*H_n)$ is defined as

$$\Delta G(*H_n) = \Delta E(*H_n) - \Delta E_{ZPE} - T\Delta S \tag{S16a}$$

$$\Delta E(*H_n) = E(*H_n) - E(*H_{n-1}) - 1/2E(H_2) \tag{S16b}$$

where $\Delta E(*H_n)$ represents the total energy change for the adsorption of the n_{th} hydrogen atom on the catalyst, ΔE_{ZPE} and ΔS are the zero-point energy and entropy change of the system. According to the literature [14], S16a can be simplified as:

$$\Delta G(^*\mathrm{H_n}) = \Delta E(^*\mathrm{H_n}) + 0.24\ \mathrm{eV} \quad \text{(S16c)}$$

Multi values of n have been examined in this study, since n reflects the hydrogen coverage (θ), which is derived as n divided by the number of original atoms in the supercell.

Figure S25 plots the $\Delta G(^*\mathrm{H_n})$ versus the adsorbed H atoms (n) in the catalyst. Clearly, the carbon atoms at the armchair edge and near the graphitic N dopants display the best HER catalytic activity when θ = 2.27% (Figure 9d).

Supplemental Experimental Data

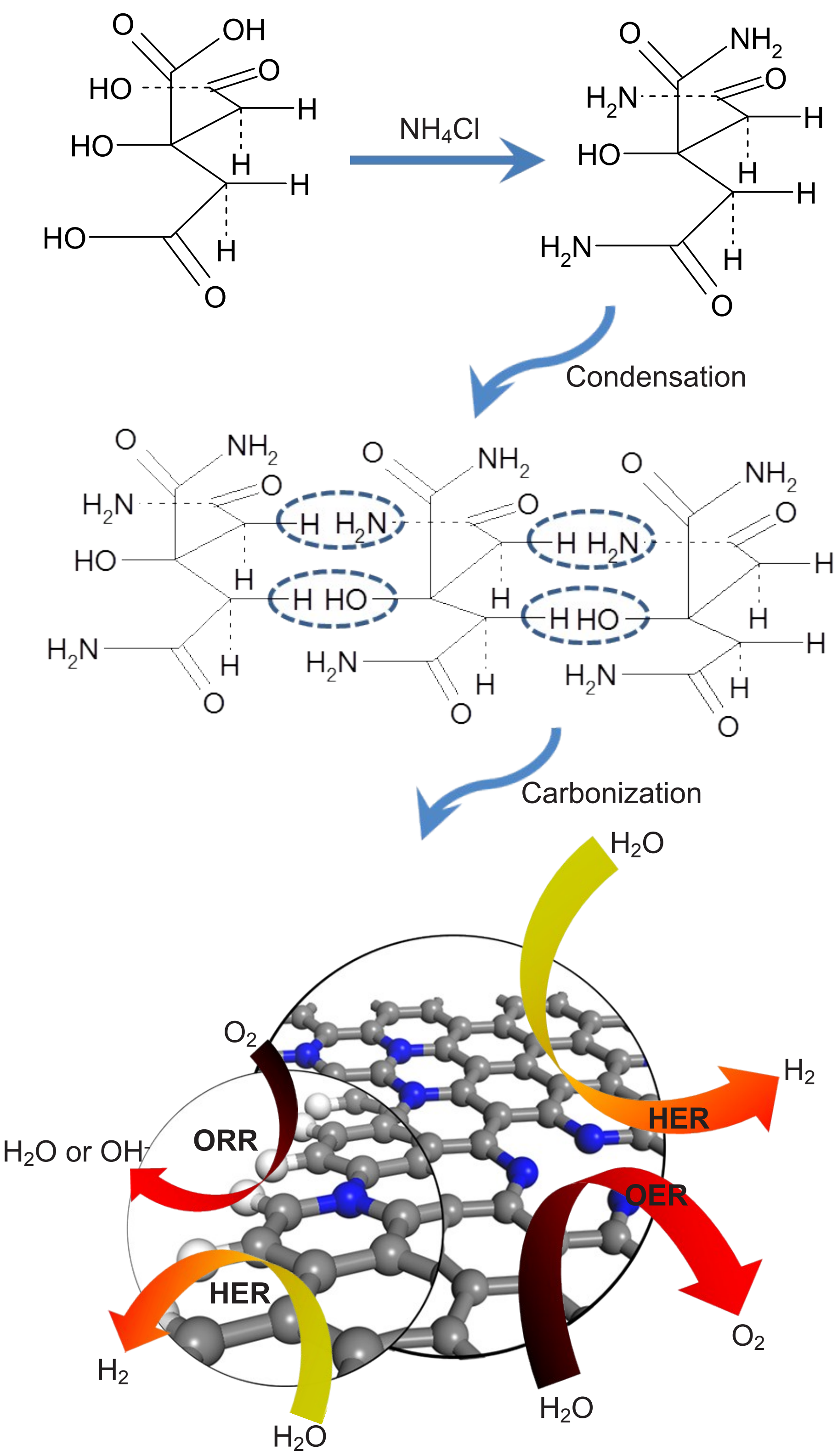

Figure S1. Schematic illustration of the preparation process for NCNs.

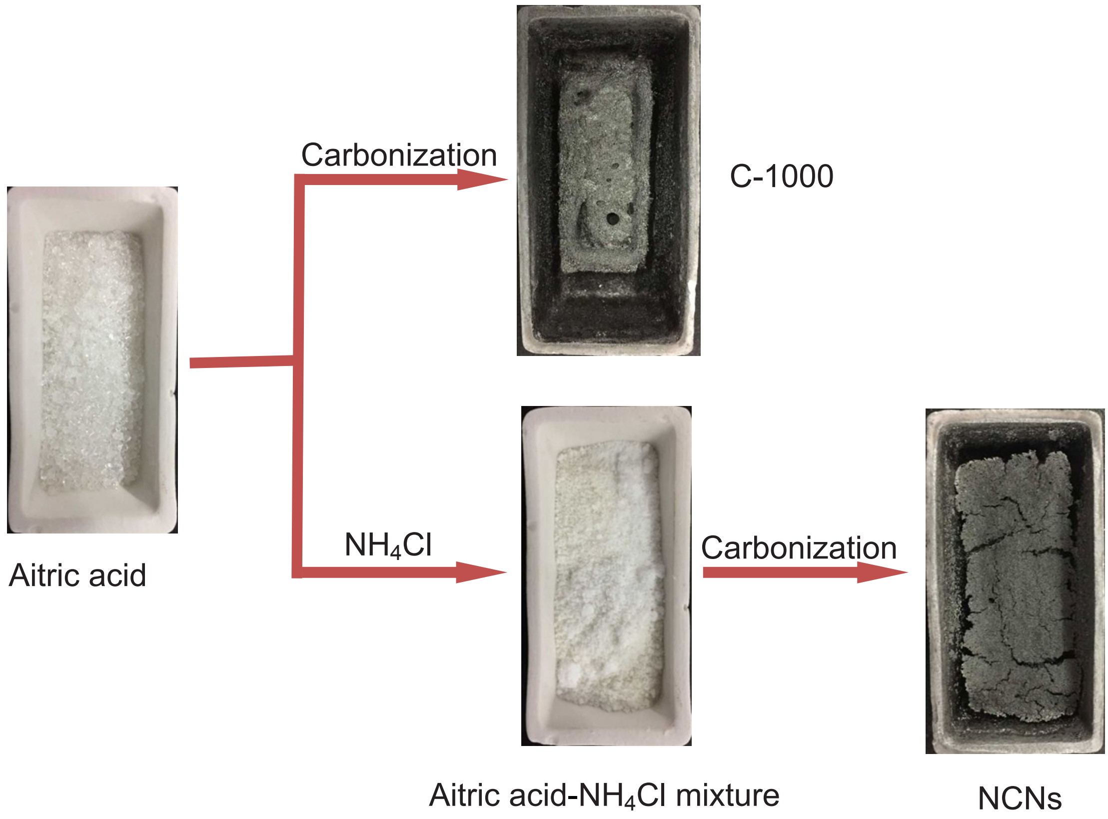

Figure S2. Optical images of the preparation process for the catalysts.

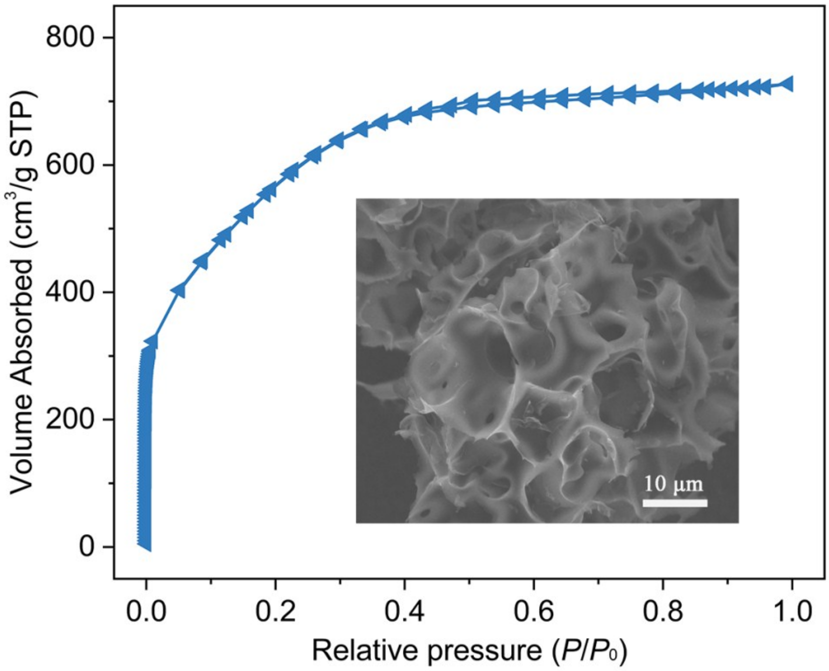

Figure S3 N_2 absorption/desorption isotherms and (inset) SEM image of 3D porous spiral polyhedron carbon structures.

Our experimental results showed that various hierarchical porous carbon materials can be obtained by simply pyrolysing the mixture of NH_4Cl and carbon precursor rich in carbon atoms and hydroxy/carboxyl groups (tartaric acid, malic acid, ascorbic acid and so on). As shown in the inset of Figure S3, 3D porous spiral polyhedron carbon structures fabricated via one-step carbonization of tartaric acid and NH_4Cl. The 3D carbon frameworks possess hierarchical macro-, meso- and microporous structures and ultrahigh specific surface area of 2034 m^2/g (Figure S3).

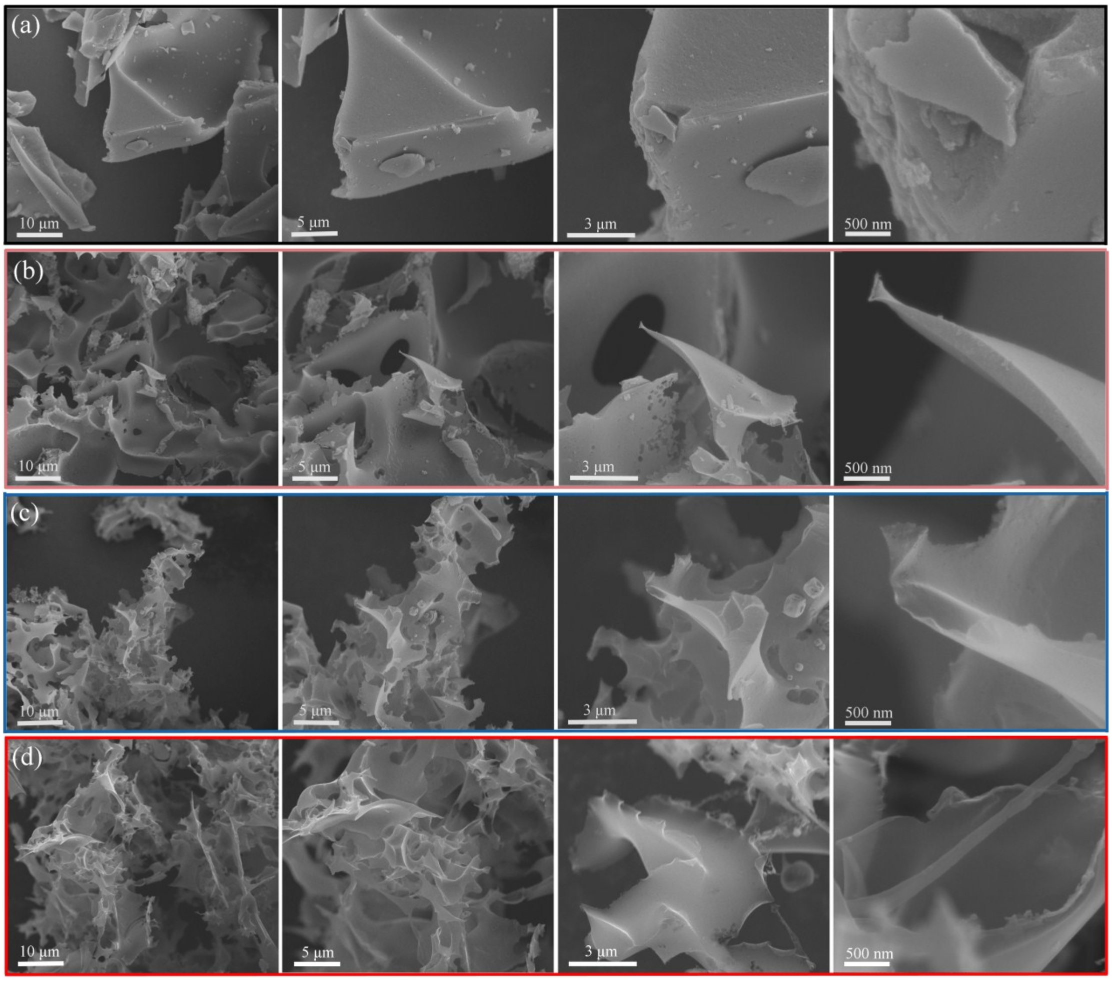

Figure S4. SEM images of (a) C-1000, (b) NCN-800-5, (c) NCN-900-5 and (d) NCN-1000-5.

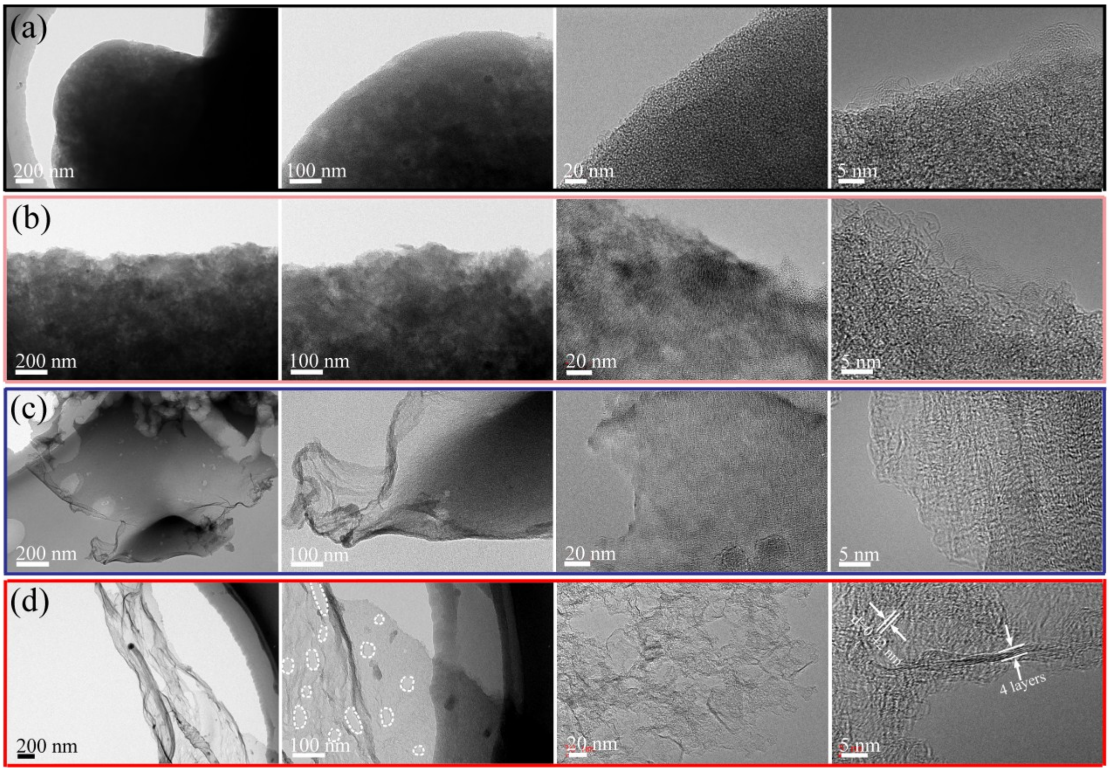

Figure S5. TEM and HRTEM images of (a) C-1000, (b) NCN-800-5, (c) NCN-900-5 and (d) NCN-1000-5.

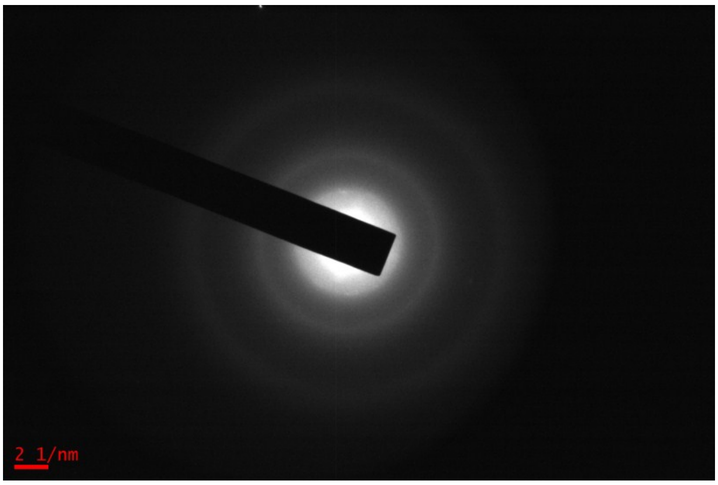

Figure S6. The selected area electron diffraction (SAED) pattern of NCN-1000-5.

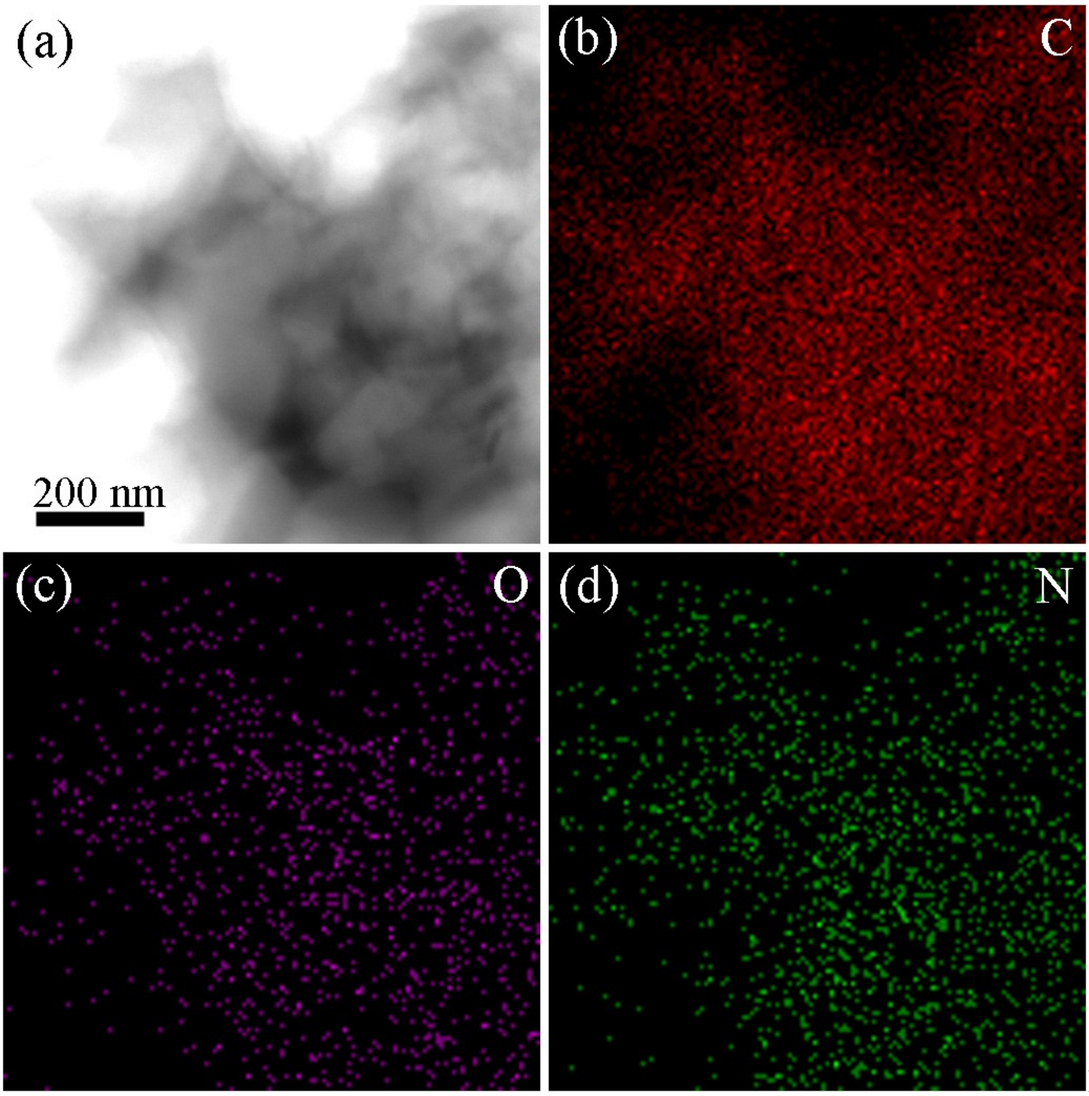

Figure S7. (a) STEM image of NCN-1000-5 and the corresponding elemental mapping images of (b) C, (c) O and (d) N elements.

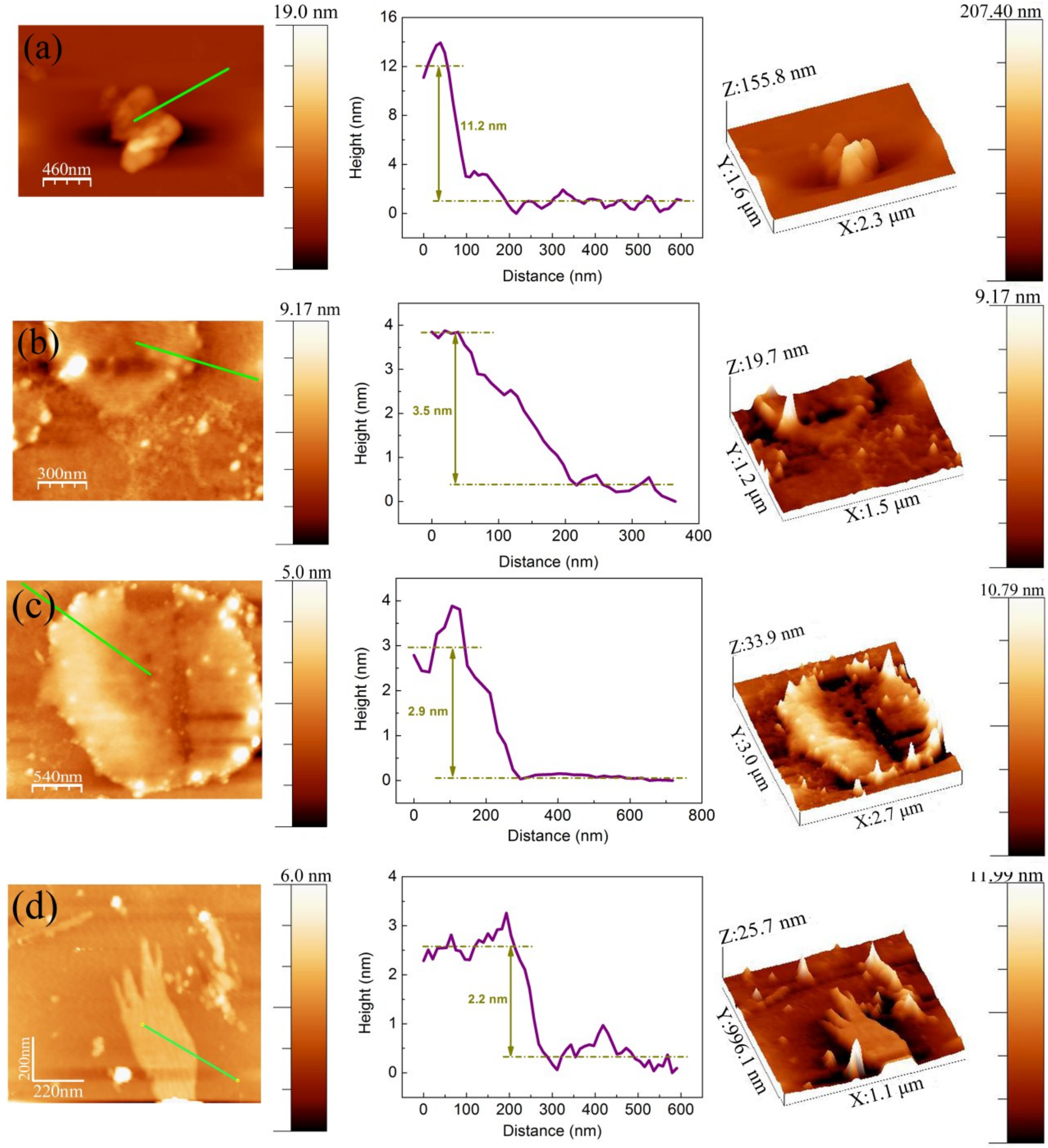

Figure S8. AFM images of (a) NCN-800-5, (b) NCN-900-5, (c) NCN-1000-2.5 and (d) NCN-1000-5.

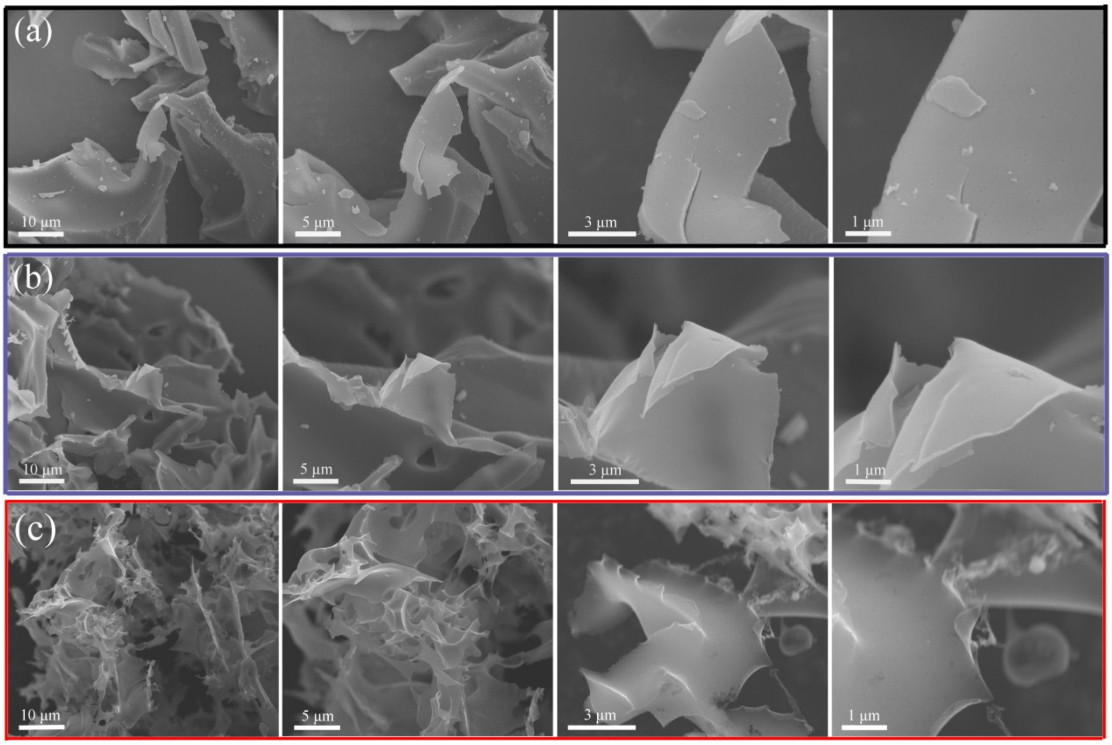

Figure S9. SEM images of (a) NCN-1000-1, (b) NCN-1000-2.5 and (c) NCN-1000-5.

Figure S9 presents the SEM images of NCNs with various mass ratios from 5:1 to 1:1 (citric acid to NH_4Cl). Note that the addition NH_4Cl is essential for the formation of carbon nanosheets and constructing cross-linked 3D porous networks. At a relatively low mass ratio of 5:1, large carbon chunk (NCN-1000-1) with highly compact texture is obtained. It is easy to find that the morphology and structure of NCN-1000-1 is rather similar to that of C-1000. With increasing the ratio to 2.5:1, the sheet-like carbons (NCN-1000-2.5) with the thickness of ~3 nm can be observed (Figure S8c and S9b). When the mass ratio is further increased to 1:1, cross-linked 3D porous carbon networks with interconnected ultrathin carbon nanosheets (NCN-1000-5) were emerged. The thickness of obtained NCNs decreased with the increase mass of NH_4Cl, which is confirmed by the AFM results (Figure S8). However, it should be noted that the thickness of NCNs can't be infinitely thinned by limitlessly increased the mass of NH_4Cl.

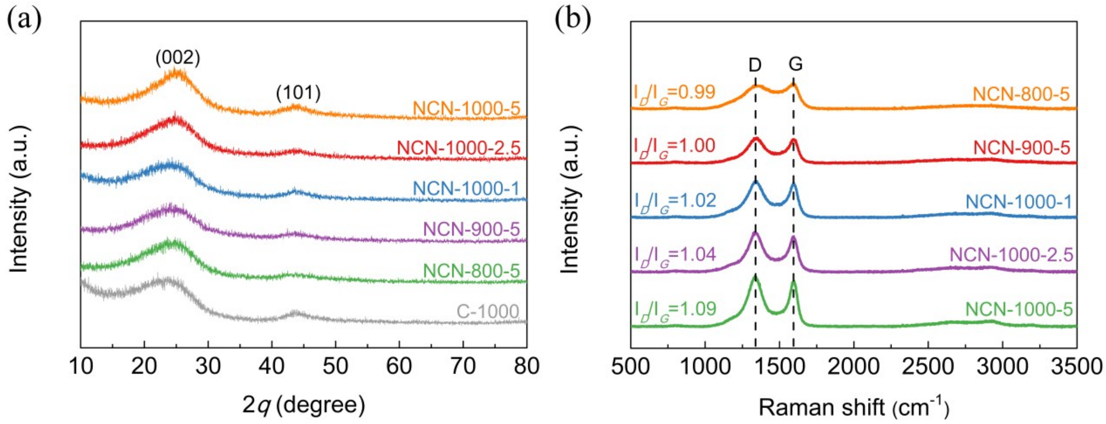

Figure S10. (a) XRD patterns and (b) Raman spectra of C-1000, NCN-800-5, NCN-900-5, NCN-1000-1, NCN-1000-2.5 and NCN-1000-5.

Table S1. BET results of the C-1000 and NCNs samples.

Samples	Specific surface area (m^2 g^{-1})	Pore volume (cm^3 g^{-1})
C-1000	37	0.097
NCN-800-5	663	0.120
NCN-900-5	1164	0.246
NCN-1000-1	969	0.118
NCN-1000-2.5	1579	0.456
NCN-1000-5	1793	0.407

Table S2. Elemental composition of the C-1000 and NCNs samples obtained from XPS results.

Sample	C (at.%)	O (at.%)	N (at.%)
C-1000	95.69	4.31	/
NCN-800-5	90.31	3.28	6.42
NCN-900-5	90.99	4.40	4.62
NCN-1000-1	94.58	3.29	2.21
NCN-1000-2.5	94.29	3.59	2.11
NCN-1000-5	93.37	4.17	2.46

Table S3. Atomic concentrations (at.%) of heterocyclic N components of NCNs samples in the N 1s binding energy region.

Samples	Pyridinic N	Pyrrolic N	Graphitic N	Oxidated N
	~398.3 eV	~399.8 eV	~401.1 eV	~402-406 eV
NCN-800-5	31.68 %	16.73 %	30.75 %	20.84 %
NCN-900-5	27.62 %	15.42 %	36.17 %	20.79 %
NCN-1000-1	14.03 %	8.96 %	53.90 %	23.11 %
NCN-1000-2.5	8.14 %	14.30 %	51.02 %	26.54 %
NCN-1000-5	16.12 %	13.45 %	50.93 %	19.50 %

Table S4. The total transition metal (Fe, Co and Ni) content of NCN-1000-5 detected by ICP-AES.

Sample	Fe (wt.%)	Co (wt.%)	Ni (wt.%)
NCN-1000-5	0.002	0.004	0.001

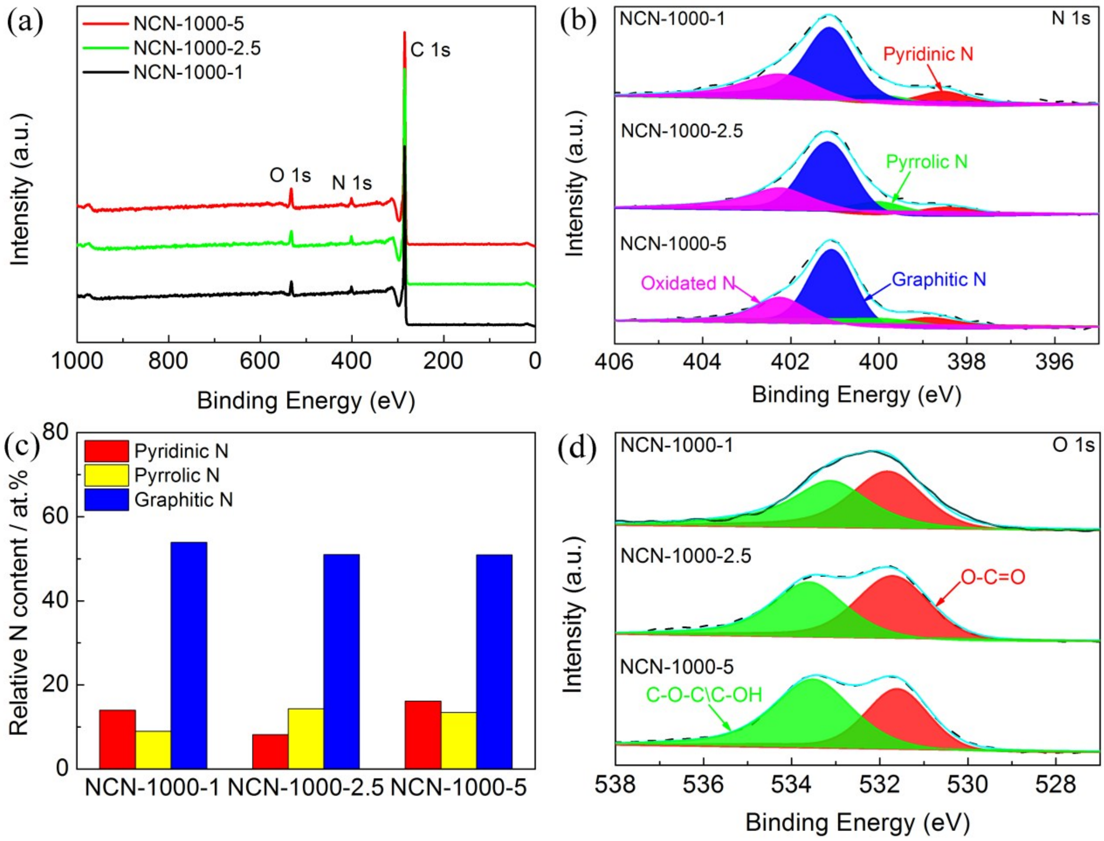

Figure S11. (a) The wide XPS survey spectra, (b) high-resolution N 1s spectra, (c) the contents of different N species and (b) high-resolution O 1s spectra of NCN-1000-1, NCN-1000-2.5 and NCN-1000-5.

According to the XPS analysis (Figure S11 and Table S3), it is easy to find that the N content in NCNs is essentially unchanged under the same pyrolysis temperature of 1000 °C, though the mass of nitrogen source is increasing. Correspondingly, the contents of nitrogen species in NCN-1000-1, NCN-1000-2.5 and NCN-1000-5 also keep almost unchanged and the graphitic N account for the largest atomic proportion at this temperature. Moreover, the O1s peaks at 531.7 and 533.3 eV (Figure S11d) are associated with oxygen in the states of O-C=O and C–O–C/C–OH, respectively.[15] Similarly to C-N, these groups (O-C=O, C–O–C and C–OH) might render adjacent carbon atoms positively charged because of the electronwithdrawing oxygen atoms in a graphite carbon π-system.[16] Thus, the presence of O atoms in NCNs may also contribute to facilitate the electrochemical reactions, especially for OER.

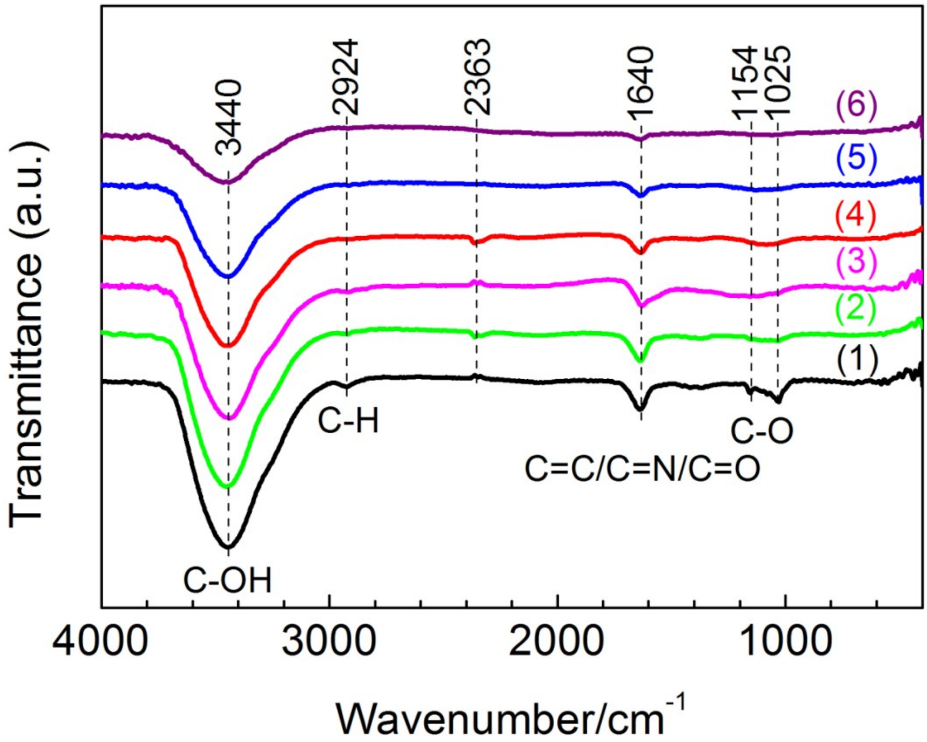

Figure S12. FT-IR spectra of (1) C-1000, (2) NCN-800-5, (3) NCN-900-5, (4) NCN-1000-5, (5) NCN-1000-2.5 and (6) NCN-1000-1.

In the FT-IR spectra of C-1000 and NCNs, the characteristic bands at 1025 and 1154 cm^{-1} were ascribed to C-O stretching vibrations, respectively, whereas the bands at 2924 and 3440cm^{-1} were related to C-H and C-OH stretching vibrations, respectively.[16] The decrease in overall intensity of the peaks with increasing carbonization temperature may be attributed to the decomposition of functional groups at a high temperature. Note that the obvious signals of C=N bond have not been detected by FT-IR, probably because of the relative low content of nitrogen in NCNs samples and the overlap of peaks for C=C (~1650 cm^{-1}), C=N (~1645 cm^{-1}) and C=O (~1640 cm^{-1}).[17]

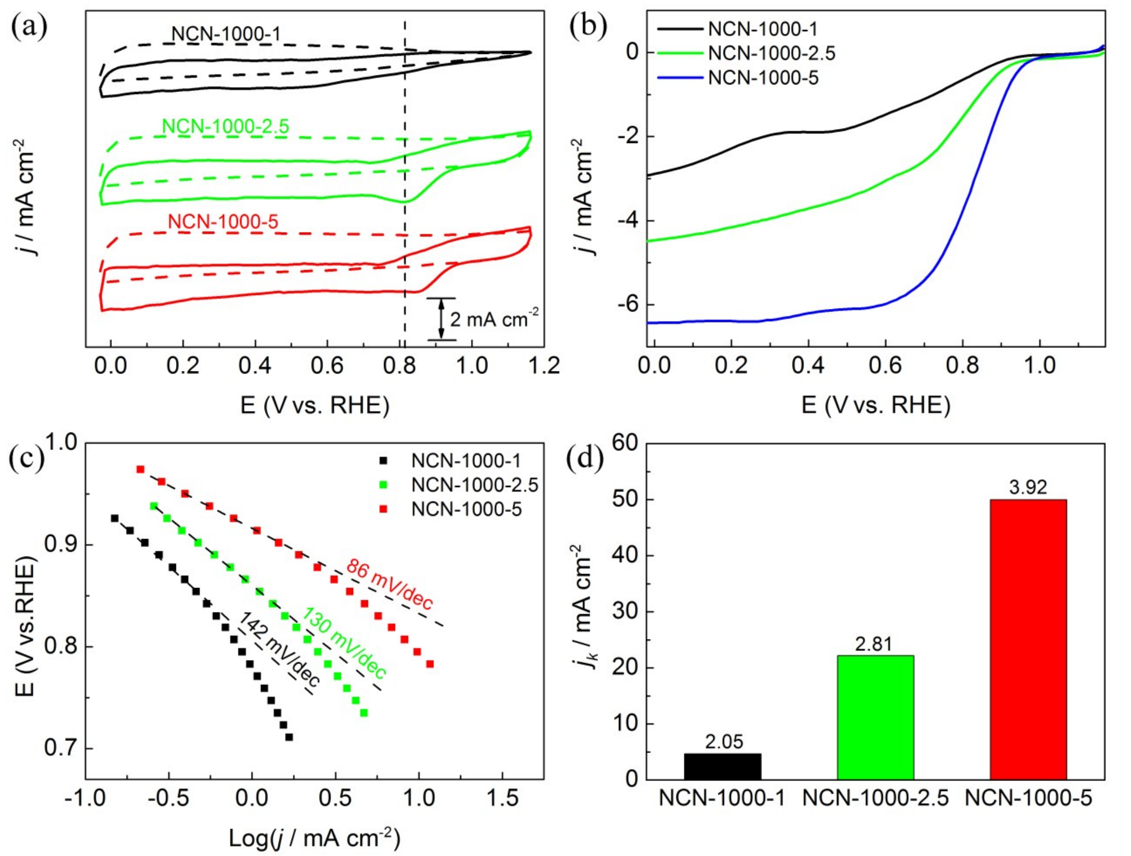

Figure S13. (a) CV, (b) LSV and (c) Tafel plots of NCN-1000-1, NCN-1000-2.5 and NCN-1000-5 in 0.1 M KOH; (d) electrochemical activity given as the kinetic current density (J_k) at 0.5 V (vs. RHE) for various catalysts, the numeral on the bar represents the corresponding electron transfer number.

Table S5. The ORR performance parameters of various samples tested in alkaline media.

Sample	E_p (V vs. RHE)	E_{onset} (V vs. RHE)	$E_{1/2}$ (V vs. RHE)	Diffusion limiting current (mA cm^{-2})
C-1000	0.49	0.67	0.32	2.77
NCN-800-5	0.57	0.79	0.56	3.35
NCN-900-5	0.75	0.88	0.71	4.85
NCN-1000-1	0.56	0.93	0.60	2.93
NCN-1000-2.5	0.81	0.94	0.75	4.49
NCN-1000-5	0.86	0.95	0.82	6.43
20% Pt/C	0.85	0.93	0.84	6.35

Table S6. Comparison of the ORR performance of NCN-1000-5 with some advanced metal-free catalysts reported in literatures in alkaline media. [a]

Catalyst	Electrolyte	Loading Mass (mg cm^{-2})	E_{onset} (V)	$E_{1/2}$ (V)	Limiting current density (mA cm^{-2})	n	Ref.
NCN-1000-5	**0.1 M KOH**	**0.20**	**0.95**	**0.82**	**6.43**	**3.92**	**This work**
NCNs	0.1 M KOH	0.28	0.95	0.83	4.61	3.70	[18]
CCa	0.1 M KOH	\	0.90	0.75	4.90	3.60	[19]
NDC-900	0.1 M KOH	0.28	0.86	0.76	4.21	3.90	[20]
NPC-1000	0.1 M KOH	0.42	1.02	0.90	5.85	3.87	[21]
N-CNTs-750	0.1 M KOH	0.31	0.85	0.75	3.19	\	[22]
N-CN9	0.1 M KOH	0.21	0.86	0.80	4.50	3.90	[23]
NCNF-1000	0.1 M KOH	0.10	0.93	0.82	4.70	4.00	[24]
3D-CNTA	0.1 M KOH	0.41	0.90	0.81	4.35	3.89	[25]
1100-CNS	0.1 M KOH	0.14	0.94	0.85	5.80	3.96	[26]
PS-CNF	0.1 M KOH	0.15	0.97	0.87	7.14	4.00	[27]
NPCN-900	0.1 M KOH	0.20	0.92	0.78	5.50	3.85	[28]
egg-CMS	0.1 M KOH	2.00	0.84	0.68	4.36	3.11	[29]
NPMC-1000	0.1 M KOH	0.15	0.94	0.85	4.24	3.85	[30]
MPSA/GO-1000	0.1 M KOH	0.30	0.89	0.82	5.06	3.70	[31]
CN_x/CS_x-GNRs	0.1 M KOH	\	0.93	0.80	2.90	3.92	[32]
SHG	0.1 M KOH	0.56	0.94	0.85	5.03	0.85	[33]
Co/CoO@Co-N-C	0.1 M KOH	0.40	0.93	0.78	7.71	3.95	[34]
NiO/CoN PINWs	0.1 M KOH	0.20	0.89	0.68	4.62	3.97	[35]
N-GCNT/FeCo-3	0.1 M KOH	0.20	1.03	0.92	5.40	3.90	[36]
CoZn-NC-700	0.1 M KOH	0.24	0.98	0.84	4.93	3.67	[37]

[a] All the potential values here are vs. RHE for comparison. In 0.1 M KOH electrolyte (pH=13), E(vs. RHE)= E(vs. Ag/AgCl) + 0.198 V + 0.059×pH= E(vs. Ag/AgCl) + 0.967 V, converted from Ag/AgCl in saturated KCl. n described here is the average electron transfer number based on the RDE result.

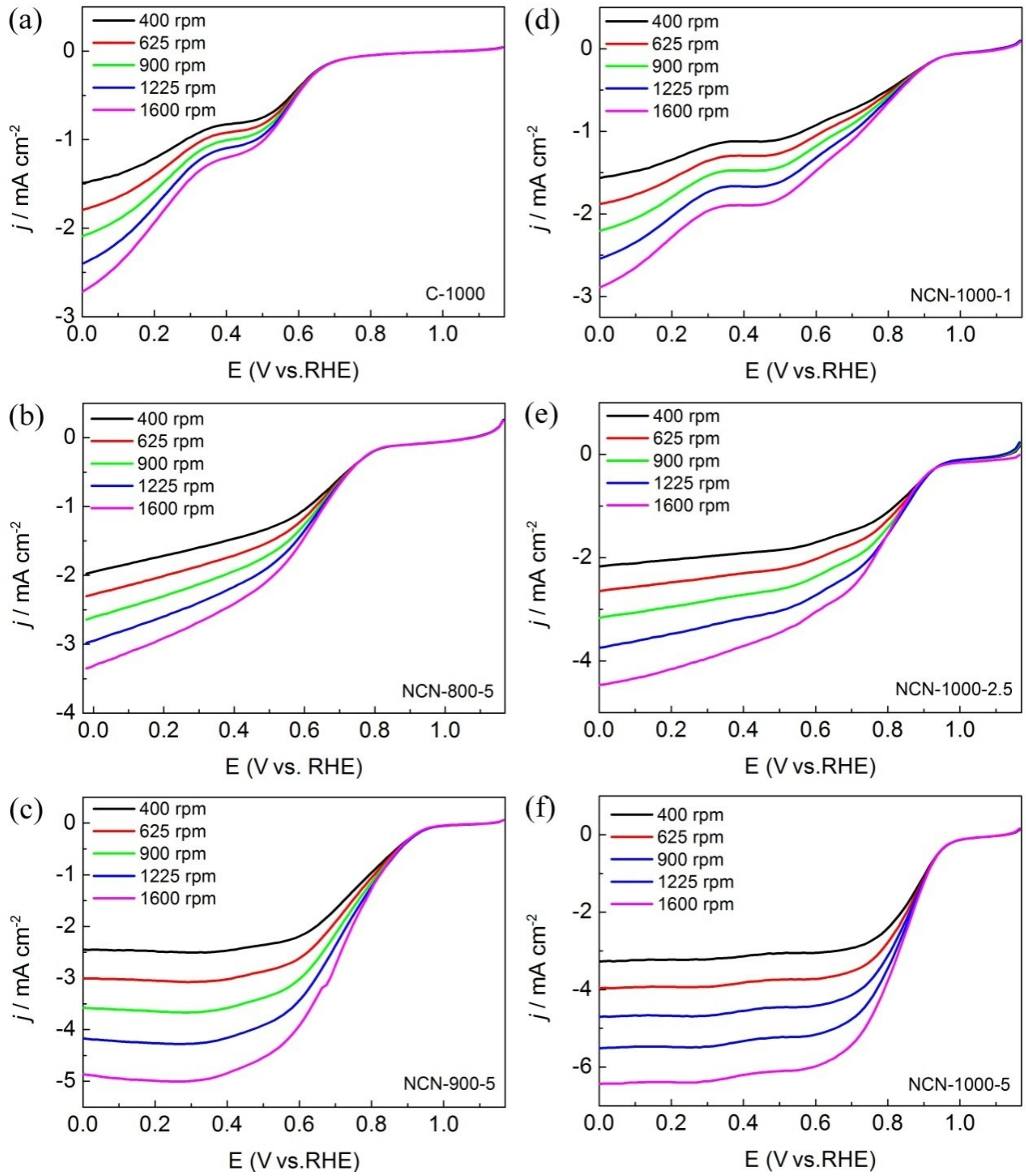

Figure S14. LSV curves at different rotating speeds for (a) C-1000, (b) NCN-800-5, (c) NCN-900-5, (d) NCN-1000-1, (e) NCN-1000-2.5 and (f) NCN-1000-5 in O_2-saturated 0.1 M KOH electrolyte (scan rate: 5 mV s^{-1}).

The LSV curves in Figure S14 revealed that the obtained current density augments with increasing rotation speeds due to their shortened diffusion distance.

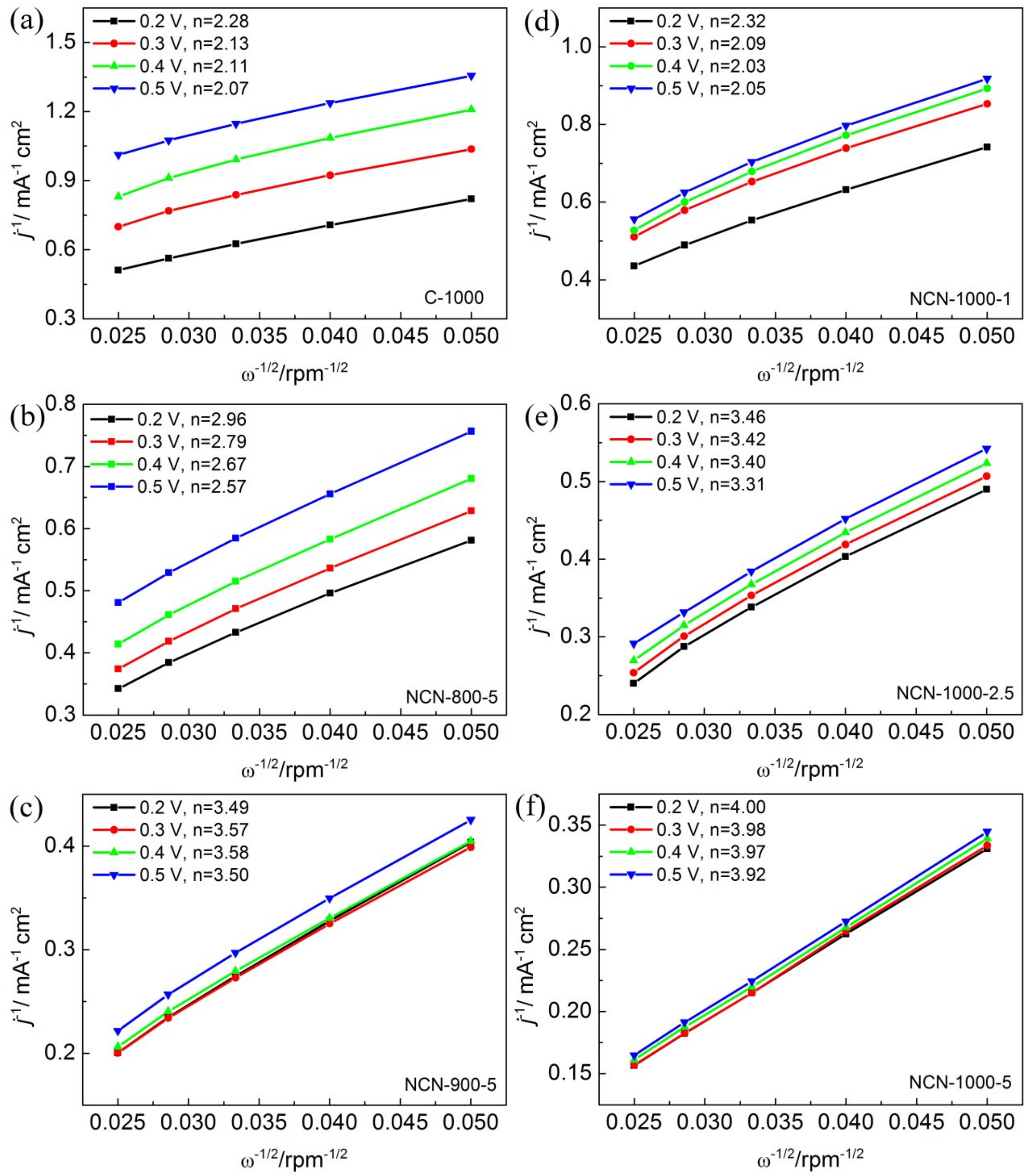

Figure S15. K-L plots at various potential for (a) C-1000, (b) NCN-800-5, (c) NCN-900-5, (d) NCN-1000-1, (e) NCN-1000-2.5 and (f) NCN-1000-5 in O_2-saturated 0.1 M KOH electrolyte.

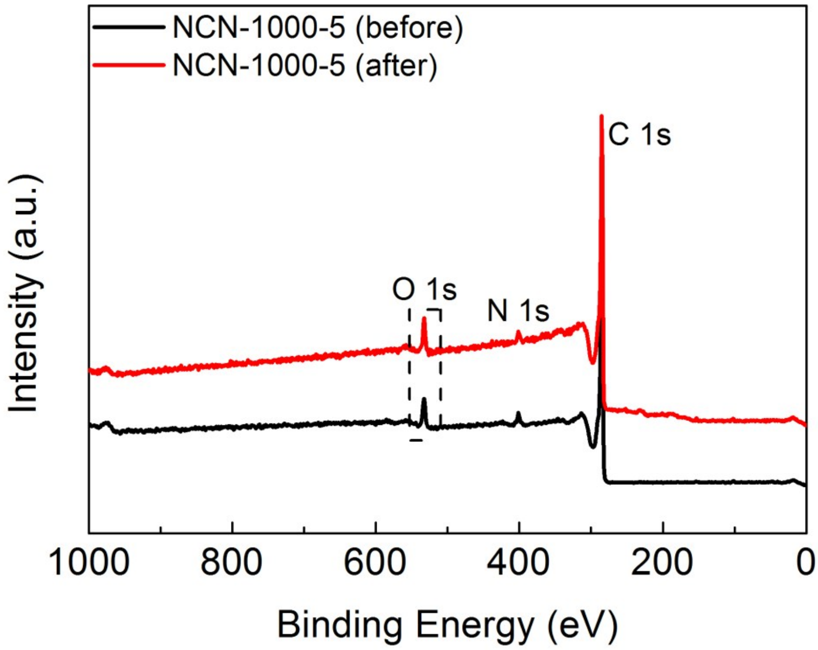

Figure S16. The wide XPS survey spectra of NCN-1000-5 before and after *i-t* measurements.

Table S7. Elemental composition of NCN-1000-5 samples before and after *i-t* measurements obtained from XPS results.

Sample	C (at.%)	O (at.%)	N (at.%)
NCN-1000-5 (before)	93.37	4.17	2.46
NCN-1000-5 (after)	91.81	6.05	2.14

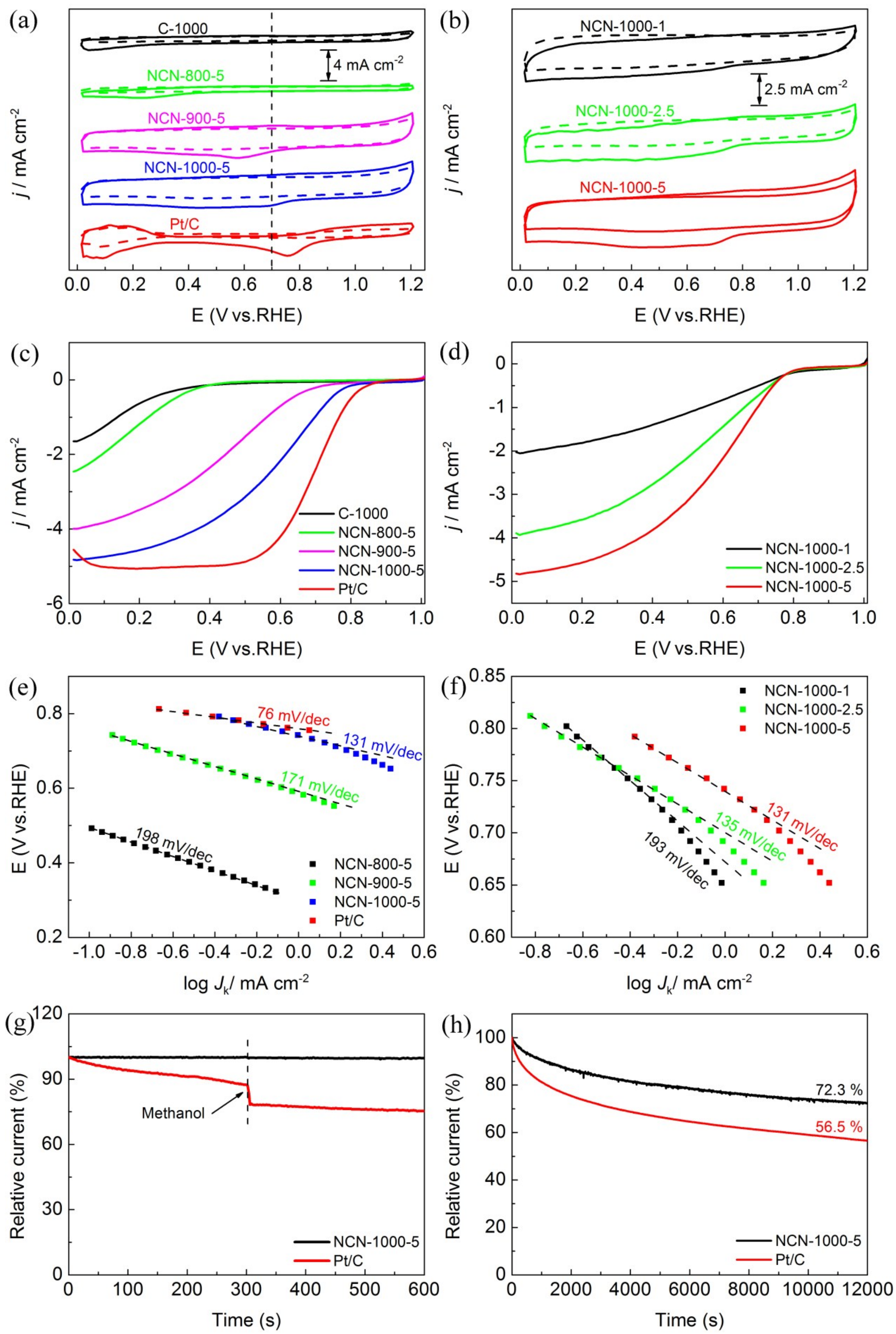

Figure S17 (a, b) CV, (c, d) LSV and (e, f) Tafel plots of C-1000, NCN-800-5, NCN-900-5, NCN-1000-1, NCN-1000-2.5, NCN-1000-5 and Pt/C in 0.5 M H_2SO_4 electrolytes; (e) methanol crossover tolerance and (f) durability tests of NCN-1000-5 and Pt/C at 0.4 V (vs. RHE) in 0.5 M H_2SO_4 electrolytes (1600 rpm).

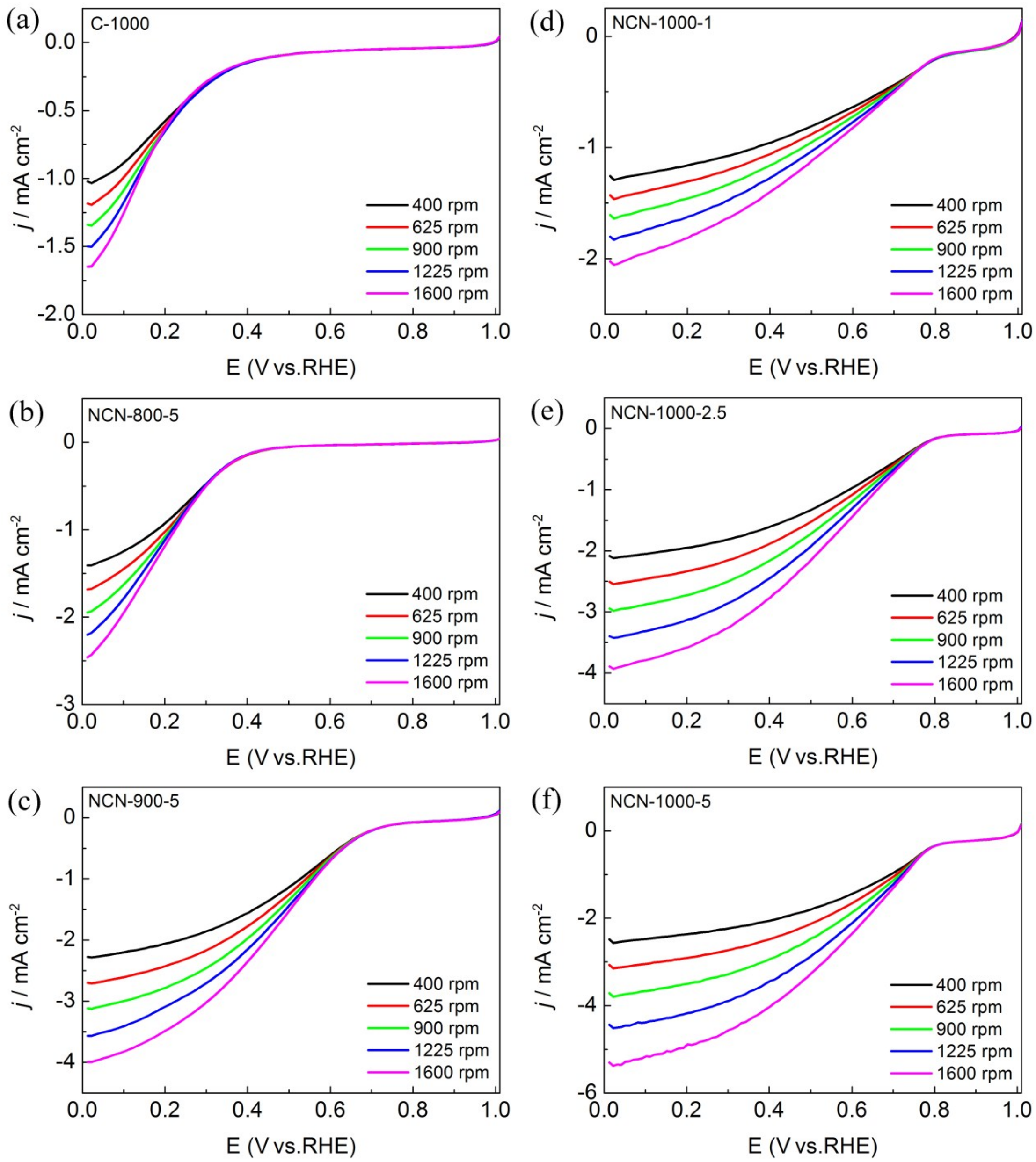

Figure S18. LSV curves at different rotating speeds for (a) C-1000, (b) NCN-800-5, (c) NCN-900-5, (d) NCN-1000-1, (e) NCN-1000-2.5 and (f) NCN-1000-5 in O_2-saturated 0.5 M H_2SO_4 electrolyte.

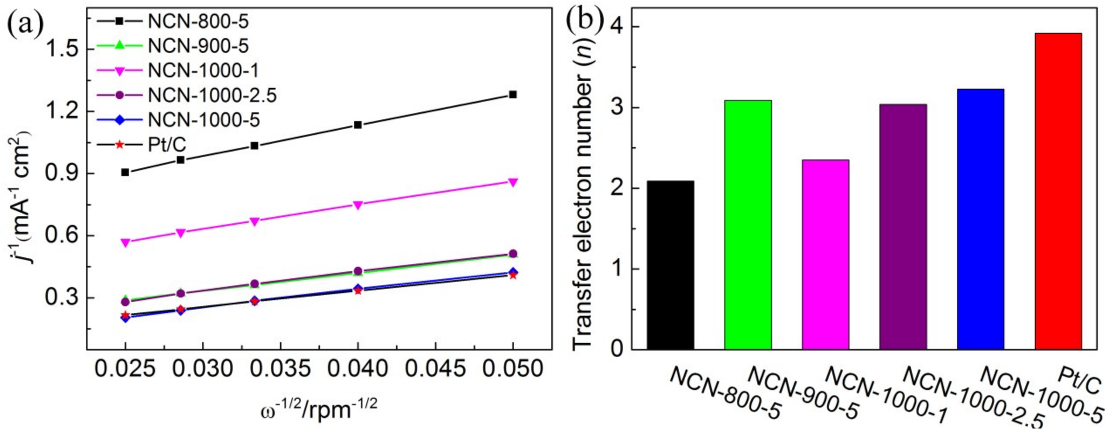

Figure S19. (a) K-L plots and (b) transfer electron numbers of NCN-800-5, NCN-900-5, NCN-1000-1, NCN-1000-2.5, NCN-1000-5 and Pt/C in O_2-saturated 0.5 M H_2SO_4 electrolyte at 0.2 V (vs. RHE).

Table S8. The ORR performance parameters of different samples tested in acidic media.

Catalyst	E_p (V vs. RHE)	E_{onset} (V vs. RHE)	$E_{1/2}$ (V vs. RHE)	Diffusion limiting current (mA cm^{-2})
C-1000	0.04	0.29	0.16	1.65
NCN-800-5	0.24	0.37	0.19	2.46
NCN-900-5	0.58	0.69	0.44	3.99
NCN-1000-1	0.38	0.78	0.54	2.03
NCN-1000-2.5	0.51	0.78	0.53	3.92
NCN-1000-5	0.70	0.78	0.58	4.82
20% Pt/C	0.76	0.80	0.69	5.05

Table S9. Comparison of the ORR performance of NCN-1000-5 with some advanced metal-free catalysts reported in literatures in acid media. [a]

Catalyst	Electrolyte	Loading Mass (mg cm^{-2})	E_{onset} (V)	$E_{1/2}$ (V)	J_L (mA cm^{-2})	n	Ref.
NCN-1000-5	**0.5 M H_2SO_4**	**0.20**	**0.78**	**0.58**	**4.82**	**3.23**	**This work**
DG	0.1 M H_2SO_4	0.28	0.59	0.36	2.50	\	[38]
NCNs	0.5 M H_2SO_4	0.28	0.75	0.66	4.20	3.90	[18]
CCa	0.5 M H_2SO_4	\	0.76	0.37	3.45	3.81	[19]
NPC-1000	0.5 M H_2SO_4	0.42	0.81	0.60	5.85	3.88	[21]
N-CNTs-750	0.5 M H_2SO_4	0.31	0.66	0.39	2.32	\	[22]
NPCN-900	0.5 M H_2SO_4	0.20	0.74	0.51	4.49	3.64	[28]
SHG	0.5 M H_2SO_4	0.56	0.87	0.76	5.00	\	[33]
CN_x/CS_x-GNRs	0.5 M H_2SO_4	\	0.63	0.39	1.82	3.32	[32]

[a] All the potential values here are vs. RHE for comparison. In 0.5 M H_2SO_4 electrolyte (pH=0.25), E(vs. RHE)= E(vs. Ag/AgCl) + 0.198 V + 0.059×pH= E(vs. Ag/AgCl) + 0.212 V, converted from Ag/AgCl in saturated KCl. n described here is the average electron transfer number based on the RDE result.

Table S10. Comparison of the OER performance of NCN-1000-5 with some advanced non-noble metal catalysts reported in literatures in alkaline media. [a]

Catalyst	Electrolyte	Loading mass (mg cm^{-2})	E_{onset} (V)	$E_{j=10}$ (V)	Tafel slope (mV dec^{-1})	Ref.
NCN-1000-5	**0.1 M KOH**	**0.20**	**1.55**	**1.64**	**142**	**This work**
DG	1.0 M KOH	0.28	1.49	1.57	97	[38]
NGSH	0.1 M KOH	0.26	1.50	1.63	83	[39]
egg-CMS	0.1 M KOH	2.00	1.51	1.54	59	[29]
N-CN9	0.1 M KOH	0.21	1.57	1.77	133	[23]
NCNF-1000	0.1 M KOH	0.10	1.43	1.84	274	[24]
3D-CNTA	1.0 M KOH	0.82	1.56	1.59	89	[25]
1100-CNS	1.0 M KOH	0.42	1.30	1.69	292	[26]
PS-CNS	0.1 M KOH	0.40	1.26	1.56	64	[27]
C_3N_4-CNT-CF	1.0 M KOH	0.50	0.52	1.60	45	[40]
SHG	0.1 M KOH	0.56	1.49	1.60	71	[33]
NPMC-1000	0.1 M KOH	0.15	1.47	1.58	193	[30]
ONPPGC/OCC	1.0 M KOH	0.14	\	1.64	84	[41]
GO-PANI31-FP	0.1 M KOH	0.20	1.62	1.81	136	[42]
Co/CoO@Co-N-C	0.1 M KOH	0.40	1.59	1.61	\	[34]
NiO/CoN PINWs	0.1 M KOH	0.20	\	1.53	35	[35]
N-GCNT/FeCo-3	0.1 M KOH	0.20	1.53	1.73	99.5	[36]
CoZn-NC-700	0.1 M KOH	0.24	\	1.62	69	[37]

[a] All the potential values here are vs. RHE for comparison. In 0.1 M KOH electrolyte (pH=13), E(vs. RHE)= E(vs. Ag/AgCl) + 0.198 V + 0.059×pH= E(vs. Ag/AgCl) + 0.967 V, converted from Ag/AgCl in saturated KCl.

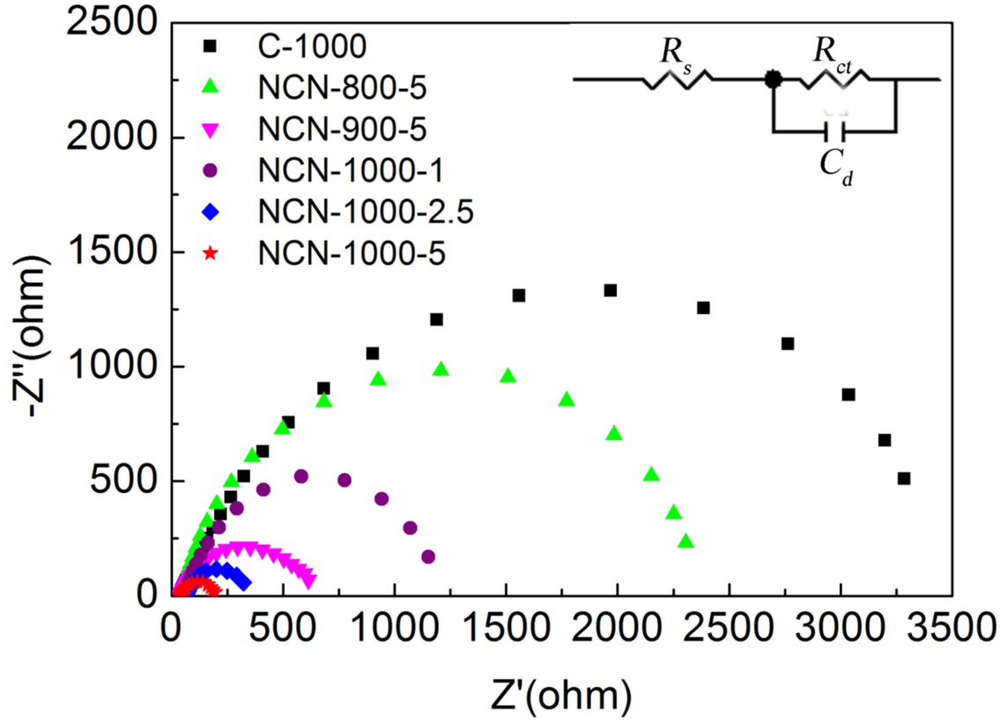

Figure S20. (a) Nyquist plots of C-1000, NCN-800-5, NCN-900-5, NCN-1000-1, NCN-1000-2.5 and NCN-1000-5, inset shows the corresponding equivalent circuit diagram.

The fitted electrochemical impedance spectroscopy (EIS) showed that the NCN-1000-5 has a smaller charge transfer resistance R_{ct} (135.9 Ω) in comparison with NCN-1000-2.5 (239.3 Ω), NCN-1000-1 (957.1 Ω), NCN-900-5 (480.3 Ω), NCN-800-5 (2004 Ω) and C-1000 (2625 Ω). The smaller charge transfer resistance clearly suggests a higher conductivity and better charge transport capability the NCN-1000-5 has. Such a low interfacial charge transfer resistance of NCN-1000-5 is mainly attributed to its ultrathin sheets structure with numerous micropores and mesopores and the moderate N doping level introduces strong electron donors into graphite structure.

Table S11. Comparison of bifunctional oxygen electrode activities of NCN-1000-5 with some noble metal-based and non-noble metal catalysts reported in literatures under the same conditions [a].

Catalyst	$E_{Onset, ORR}$, (V)	E_{ORR} (V) at -3 mA cm^{-2}	$E_{Onset, OER}$, (V)	E_{OER} (V) at 10 mA cm^{-2}	ΔE (V)	Ref.
NCN-1000-5	**0.95**	**0.83**	**1.55**	**1.64**	**0.81**	**This work**
IrO_2/C	0.65	0.30	1.34	1.69	1.39	[43]
egg-CMS	0.84	0.62	1.51	1.54	0.92	[29]
N-CN9	0.86	0.79	1.57	1.77	0.98	[23]
NCNF-1000	0.93	0.80	1.43	1.84	1.04	[24]
3D-CNTA	0.90	0.76	1.56	1.59	0.83	[25]
1100-CNS	0.95	0.84	1.30	1.69	0.85	[26]
PS-CNS	0.97	0.87	1.26	1.56	0.69	[27]
NGSH	088	0.64	1.50	1.63	0.99	[39]
SHG	0.94	0.85	1.49	1.60	0.75	[33]
NPMC-1000	0.94	0.82	1.47	1.58	0.76	[30]
Co/CoO@Co-N-C	0.92	0.79	1.59	1.61	0.82	[34]
CoO@N/S-CNF	0.84	0.65	1.53	1.61	0.96	[44]
Co-NC@CoP-NC	0.86	0.76	\	1.56	0.80	[45]
CoO@Co/N-rGO	0.95	0.74	1.53	1.65	0.91	[46]
NiO/CoN PINWs	0.89	0.65	\	1.53	0.88	[35]
Ni_3Fe/C	0.90	0.78	1.54	1.60	0.82	[43]
N-GCNT/FeCo-3	1.03	0.90	1.53	1.73	0.83	[36]
CoZn-NC-700	0.98	0.82	\	1.62	0.80	[37]

[a] All the potential values here are vs. RHE for comparison. In 0.1M KOH electrolyte (pH=13), E(vs. RHE)= E(vs. Ag/AgCl) + 0.198 V + 0.059×pH= E(vs. Ag/AgCl) + 0.967 V, converted from Ag/AgCl in saturated KCl.

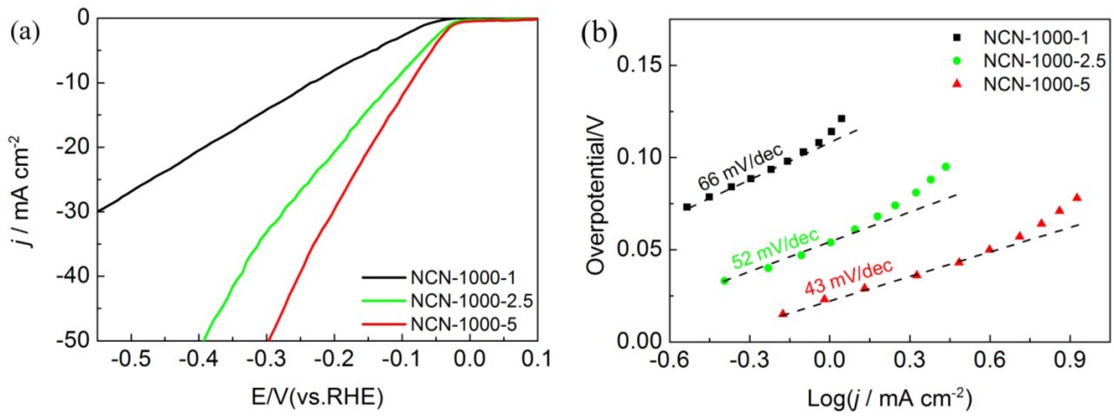

Figure S21. (a) LSV curves and (b) Tafel plots of NCN-1000-1, NCN-1000-2.5 and NCN-1000-5 in in N_2-saturated 0.5 M H_2SO_4 electrolyte (sweep rate: 5 mV s^{-1}).

Table S12. Comparison of the HER performance of NCN-1000-5 with some metal-free catalysts reported in literatures in acid media. [a]

Catalyst	Electrolyte	Loading Mass (mg cm^{-2})	E_{onset} (V)	$E_{j=10}$ (V)	Tafel slope (mV dec^{-1})	Ref.
NCN-1000-5	**0.5 M H_2SO_4**	**0.20**	**-0.03**	**-0.09**	**43**	**This work**
DG	0.5 M H_2SO_4	0.28	-0.10	-0.15	55	[38]
SHG	0.5 M H_2SO_4	0.57	-0.21	-0.27	112	[33]
NDC-900	1.0 M H_2SO_4	0.28	-0.12	-0.28	94	[20]
NC	0.5 M H_2SO_4	\	-0.06	-0.14	132	[47]
B-SuG	0.5 M H_2SO_4	\	-0.38	-0.44	99	[48]
C_3N_4-CNT-CF	0.5 M H_2SO_4	0.50	-0.15	-0.24	82	[40]
g-C_3N_4@S-Se-pGr	0.5 M H_2SO_4	0.10	-0.09	-0.30	86	[49]
ONPPGC/OCC	0.5 M H_2SO_4	0.14	-0.33	-0.38	109	[41]
MPSA/GO-1000	0.5 M H_2SO_4	0.30	-0.06	-0.16	59	[31]

[a] All the potential values here are vs. RHE for comparison. In 0.5 M H_2SO_4 electrolyte (pH=0.25), E(vs. RHE)= E(vs. Ag/AgCl) + 0.198 V + 0.059 pH= E(vs. Ag/AgCl) + 0.212 V, converted from Ag/AgCl in saturated KCl.

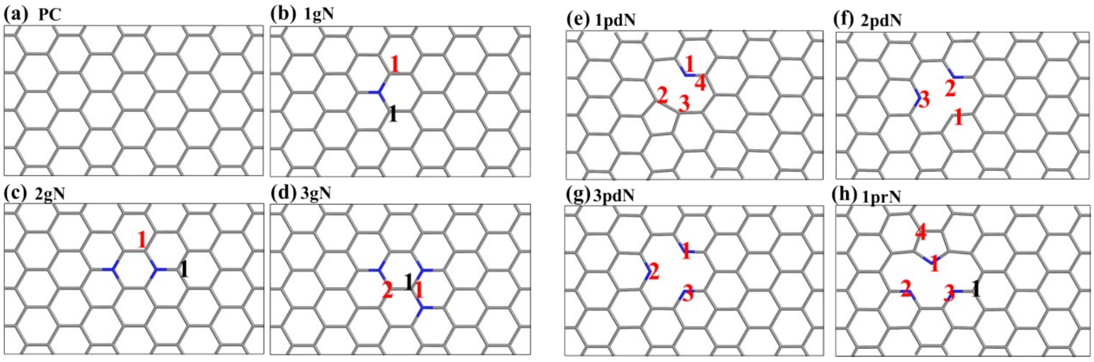

Figure S22 Models of N-doped graphene nanosheet; the potential ORR/OER active sites are labeled by black numbers, while the potential active sites for HER are labeled by red numbers.

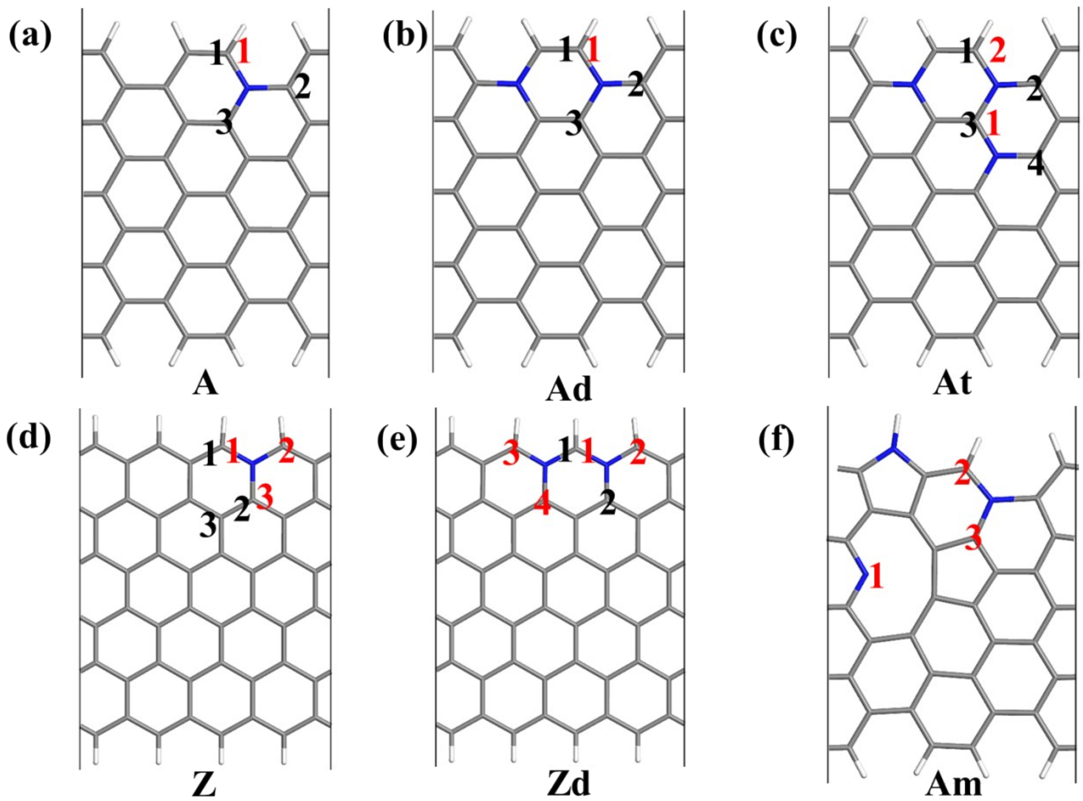

Figure S23. Models of N-doped graphene nanoribbon. The potential ORR/OER active sites are labeled by black numbers according to the distance away from the edge, while the red numbers indicate the position of the n_{th} adsorbed H atom.

Table S13. The calculated free adsorption energies of O-containing intermediates in various models.

Models	ΔG(*O)/eV	ΔG(*OH)/eV	ΔG(*OOH)/eV
PC	3.82	2.31	4.72
1gN-1	2.44	1.44	4.34
2gN-1	2.04	1.24	4.29
3gN-1	0.35	0.51	3.66
1pdN-1	3.34	2.32	4.86
1prN-2	3.48	1.30	4.99
A-1	1.77	0.78	3.91
A-2	2.35	1.38	4.32
A-3	2.51	1.16	4.24
Z-1	1.17	0.56	3.64
Z-2	2.36	1.46	4.54
Z-3	3.50	2.19	4.57
Ad-1	1.14	1.00	4.09
Ad-2	2.03	1.57	4.33
Ad-3	1.60	1.14	4.25
At-1	0.99	0.63	3.70
At-3	0.31	0.42	3.54
At-4	1.21	0.85	3.93
Zd-1	0.16	0.23	3.41
Zd-2	1.80	1.20	4.24

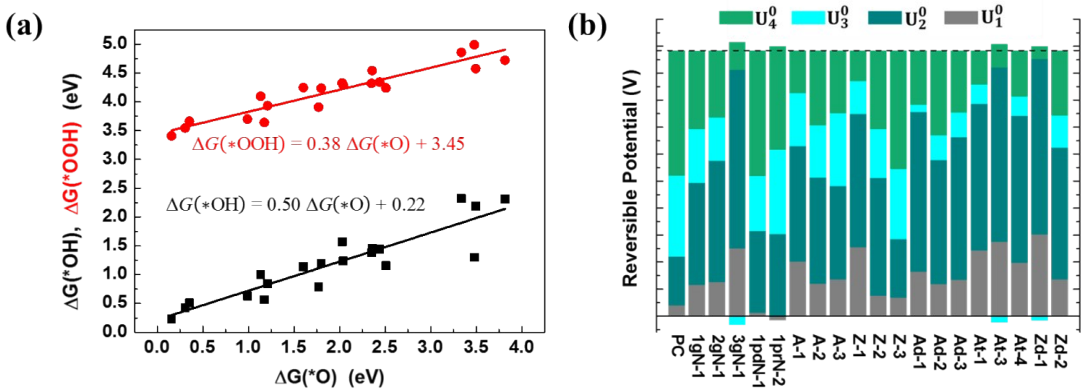

Figure S24. (a) The scaling relationship between Δ*G*(*OOH), Δ*G*(*OH) and Δ*G*(*O). (b) The plot of reversible potential of each step for selected active sites.

The black line indicates the potential of redox O_2/H_2O, which is 1.23 V. The potential determining step (PDS) for OER on different sites is mainly the reverse step of S7b (red column), excluding PC, 1pdN-1, 1prN-2, and Z-3, demonstrating that the transformation from intermediate *O to *OOH is rather difficult for OER. While for ORR, the PDS is mainly the step of S7a (black column) in active sites, such as PC, 1gN-1, 1pdN-1, 1prN-2, Z-2~3 and A-2~3, which indicates that adsorbing O_2 to form *OOH is rather difficult. Moreover, the PDS is also affected by the doping concentration and the distance for the active site away from the edge. For example, as the graphitic N doping concentration increases in graphene nanosheet (1gN-1, 2gN-1, 3gN-1) and nanoribbon (A-1, Ad-1, At-1), the PDS changes from S7a to S7c and from S7d to S7c, respectively; as the active site is further away from the edge (A-1~3 and Z-1~3), the PDS changes from S7c to S7a.

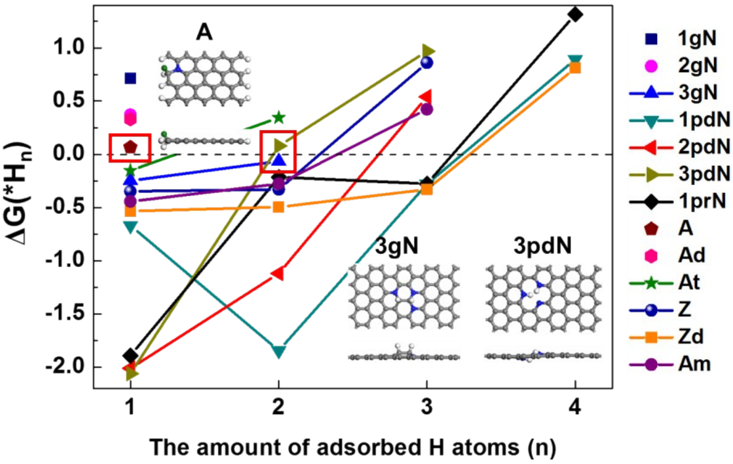

Figure S25. Differential Gibbs free energy $\Delta G(*H_n)$ as the function of the adsorbed H atoms (n) in various models. The inserted graphs sketch the optimal active sites for HER.

The graphitic N dopants near the armchair edges of micropores greatly enhance the activity of surrounding atoms. For instance, the A-1 active site, which also performs best for ORR, exhibits the highest HER catalytic activity with the Gibbs free energy of 0.07 eV at low hydrogen coverage (n = 1, θ = 2.27%). To investigate the HER catalytic performance at higher hydrogen coverage, we added more H atoms to the models whose $\Delta G(*H_n)$ is negative at n = 1, and found that two more models are also active for HER, namely 3gN and 3pdN monolayers, whose $\Delta G(*H_2)$ values are -0.07 and 0.08 eV at the hydrogen coverage of 3.12% and 3.17%, respectively.

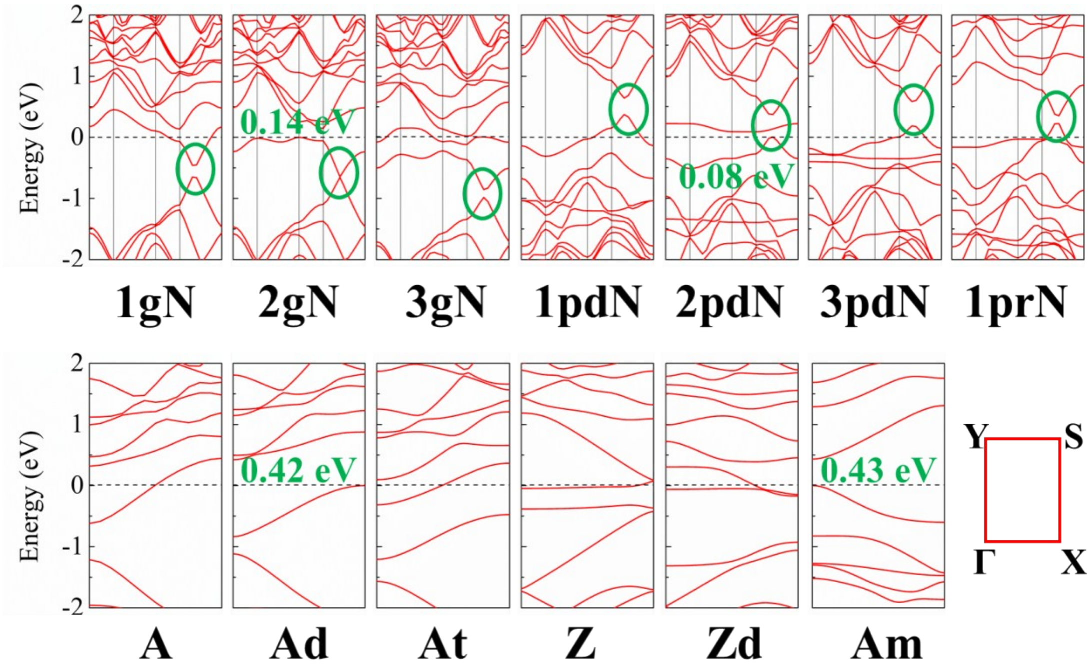

Figure S26. The band structures of thirteen models (except for pristine graphene which is semimetal with one Dirac cone at the Fermi level).

The high symmetry points from left to right are Γ-X-S-Y- Γ for N-doped graphene nanosheets, and Γ-X for N-doped graphene nanoribbon. The energy windows are set from -2 to 2 eV, where the Fermi levels (dash lines) are set to 0. Several models are semiconductor, and their band gaps are labeled by green numbers. In N-doped graphene nanosheets, the bands originated from graphene Dirac cone are circled in green for easier identification. Generally, though several N-doped graphene nanosheets/nanoribbons are semi-conductor with band gaps smaller than 0.5 eV, most local structures of N-doped graphene nanosheets are metallic, regardless of the doping type. Therefore, the synthesized N-doped carbon nanosheets material are expected to be highly conductive and can serve as good electrode materials. The graphitic N doping is *n*-type doping, since it moves the Fermi level higher than the Dirac cone bands. As the doping concentration increases from 1gN to 3gN, the Fermi level becomes even higher in energy. While pyridinic and pyrrolic N doping is *p*-type doping, since the Fermi level is pushed below the Dirac cone bands.

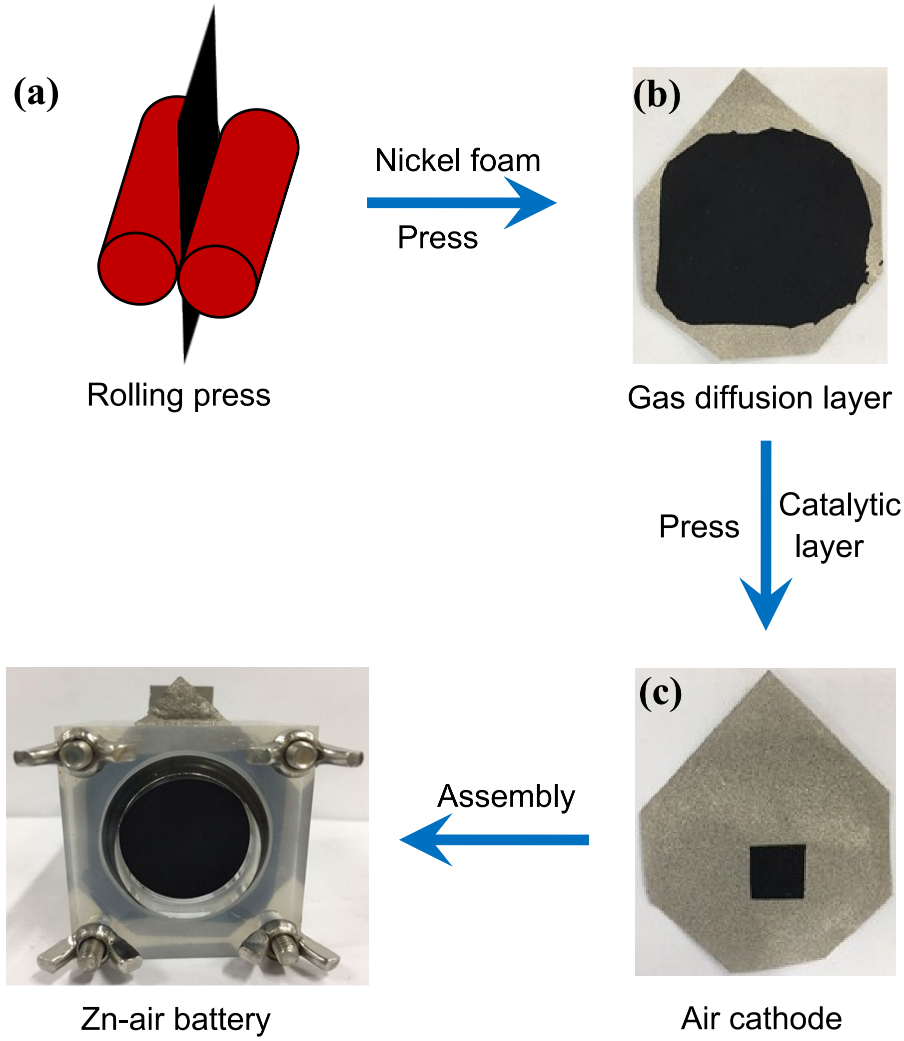

Figure S27. (a) Schematic representation of the preparation of the gas diffusion layer; photographs of (b) gas diffusion layer, (c) air-cathode loaded with catalysts and (d) primary Zn-air battery.

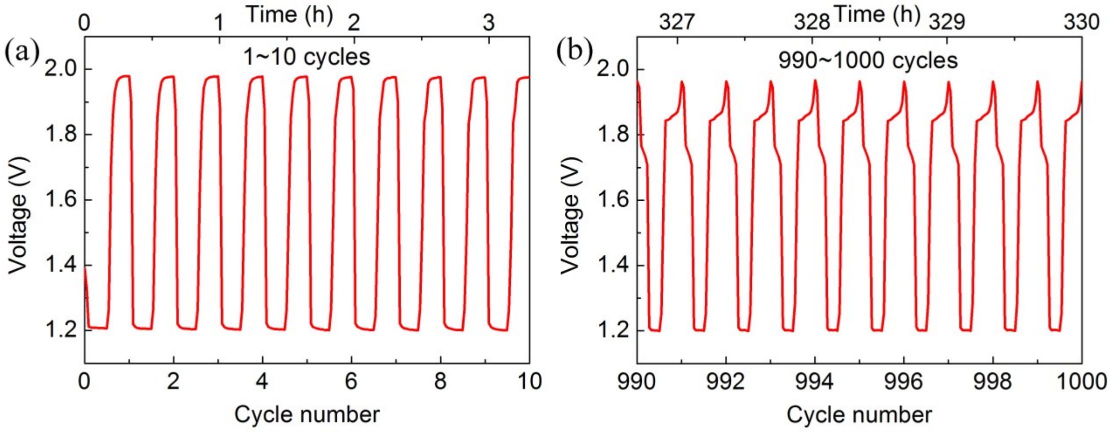

Figure S28. (a) 1~10 and (b) 900~1000 cycles discharge/charge cycling curves of Zn-air battery based on NCN-1000-5 catalyst at 10 mA cm^{-2}.

At a constant current density of 10 mA cm^{-2}, the initial charge/discharge round-trip efficiency is 61.1 %. After 1000 continuous charge/discharge cycles (about 330 h), the round-trip efficiency maintains almost unchanged.

Table S14. The performance of rechargable Zn-air batteries with various reported electrocatalys.

Catalyst	Loading (mg cm^{-2})	Voltage @ 10 mA cm^{-2} (V)	Peak power density (mW cm^{-2})	Energy density (Wh kg^{-1})	Initial round-trip efficiency	Cycling conditions and stability	Ref.
NCN-1000-80	**2.0**	**1.21**	**207**	**806**	**61.1 %**	**10 mA cm^{-2}, 20 min/cycle for 1000 cycles; no obvious voltage decay**	**This work**
Pt/C+RuO_2	2.0	1.25	196	890	62.2 %	10 mA cm^{-2}, 20 min/cycle for 436 cycles; voltage gap increased ~0.47 V	This work
N-CN9	1.0	1.10	41	\	52.7 %	10 mA cm^{-2}, 10 min/cycle for 30 cycles; voltage gap increased ~0.33 V	[23]
NCNF-1000	2.0	1.20	185	\	62.1 %	10 mA cm^{-2}, 10 min/cycle for 500 cycles; voltage gap increased ~0.13 V	[24]
3D-CNTA	2.0	1.31	157	\	65.8 %	10 mA cm^{-2}, 10 min/cycle for 240 cycles; voltage gap increased ~0.14 V	[25]
1100-CNS	2.0	1.25	151	\	61.0 %	10 mA cm^{-2}, 11 min/cycle for 300 cycles; voltage gap increased ~0.08 V	[26]
PS-CNS	\	1.25	231	785	62.0 %	2 mA cm^{-2}, 12 min/cycle for 600 cycles; no obvious voltage decay	[27]
Co/CoO@Co-N-C	2.0	1.25	157	\	65.1 %	10 mA cm^{-2}, 10 min/cycle for 100 cycles; voltage gap increased ~0.19 V	[34]
NiO/CoN PINWs	\	0.19	80	836	37.5 %	3 mA cm^{-2}, 10 min/cycle for 50 cycles; voltage gap increased ~0.25 V	[35]
Ni_3Fe/N-C	2.0	1.20	\	634	61.4%	10 mA cm^{-2}, 4 h/cycle for 105 cycles; oltage gap increased ~0.20 V	[43]
N-GCNT/FeCo-3	2.0	1.26	89	653	81.9 %	20 mA cm^{-2}, 20 min/cycle for 27 cycles; voltage gap increased ~0.03 V	[36]
CoZn-NC-700	1.2	1.22	152	694	63.0 %	10 mA cm^{-2}, 10 min/cycle for 385 cycles; voltage gap increased ~0.37 V	[37]

Supplementary References

[1] Delley B. From molecules to solids with the DMol[3] approach. The Journal of Chemical Physics. 2000;113(18):7756-64.

[2] Perdew JP, Burke K, Ernzerhof M. Generalized Gradient Approximation Made Simple. Phys Rev Lett. 1996;77(18):3865-8.

[3] Delley B. An all-electron numerical method for solving the local density functional for polyatomic molecules. The Journal of Chemical Physics. 1990;92(1):508-17.

[4] Grimme S. Semiempirical GGA-type density functional constructed with a long-range dispersion correction. J Comput Chem. 2006;27(15):1787-99.

[5] Man IC, Su H-Y, Calle-Vallejo F, Hansen HA, Martínez JI, Inoglu NG, et al. Universality in Oxygen Evolution Electrocatalysis on Oxide Surfaces. ChemCatChem. 2011;3(7):1159-65.

[6] Nørskov JK, Rossmeisl J, Logadottir A, Lindqvist L, Kitchin JR, Bligaard T, et al. Origin of the Overpotential for Oxygen Reduction at a Fuel-Cell Cathode. The Journal of Physical Chemistry B. 2004;108(46):17886-92.

[7] Li M, Zhang L, Xu Q, Niu J, Xia Z. N-doped graphene as catalysts for oxygen reduction and oxygen evolution reactions: Theoretical considerations. J Catal. 2014;314:66-72.

[8] Lim D-H, Wilcox J. Mechanisms of the Oxygen Reduction Reaction on Defective Graphene-Supported Pt Nanoparticles from First-Principles. The Journal of Physical Chemistry C. 2012;116(5):3653-60.

[9] Liang W, Chen J, Liu Y, Chen S. Density-Functional-Theory Calculation Analysis of Active Sites for Four-Electron Reduction of O_2 on Fe/N-Doped Graphene. ACS Catalysis. 2014;4(11):4170-7.

[10] Rossmeisl J, Logadottir A, Nørskov JK. Electrolysis of water on (oxidized) metal surfaces. Chem Phys. 2005;319(1):178-84.

[11] Abild-Pedersen F, Greeley J, Studt F, Rossmeisl J, Munter TR, Moses PG, et al. Scaling Properties of Adsorption Energies for Hydrogen-Containing Molecules on Transition-Metal Surfaces. Phys Rev Lett. 2007;99(1):016105.

[12] Koper MTM. Thermodynamic theory of multi-electron transfer reactions: Implications for electrocatalysis. J Electroanal Chem. 2011;660(2):254-60.

[13] Parsons R. The rate of electrolytic hydrogen evolution and the heat of adsorption of hydrogen. Transactions of the Faraday Society. 1958;54(0):1053-63.

[14] Nørskov JK, Bligaard T, Logadottir A, Kitchin JR, Chen JG, Pandelov S, et al. Trends in the Exchange Current for Hydrogen Evolution. J Electrochem Soc. 2005;152(3):J23-J6.

[15] Yang Z, Xu M, Liu Y, He F, Gao F, Su Y, et al. Nitrogen-doped, carbon-rich, highly photoluminescent carbon dots from ammonium citrate. Nanoscale. 2014;6(3):1890-5.

[16] Chen S, Duan J, Jaroniec M, Qiao S-Z. Nitrogen and Oxygen Dual-Doped Carbon Hydrogel Film as a Substrate-Free Electrode for Highly Efficient Oxygen Evolution Reaction. Adv Mater. 2014;26(18):2925-30.

[17] Sharma R, Kar KK. Effects of surface roughness and n-content on oxygen reduction reaction activity for the carbon-based catalyst derived from poultry featherfiber. Electrochim Acta. 2016;191:876-86.

[18] Zhao Q, Ma Q, Pan F, Wang Z, Yang B, Zhang J, et al. Facile synthesis of nitrogen-doped carbon nanosheets as metal-free catalyst with excellent oxygen reduction performance in alkaline and acidic media. J Solid State Electrochem. 2016;20(5):1469-79.

[19] Ferrero GA, Fuertes AB, Sevilla M, Titirici M-M. Efficient metal-free N-doped mesoporous carbon catalysts for ORR by a template-free approach. Carbon. 2016;106:179-87.

[20] Singh DK, Jenjeti RN, Sampath S, Eswaramoorthy M. Two in one: N-doped tubular carbon nanostructure as an efficient metal-free dual electrocatalyst for hydrogen evolution and oxygen reduction reactions. J Mater Chem A. 2017;5(13):6025-31.

[21] Ye L, Chai G, Wen Z. Zn‐MOF‐74 Derived N‐Doped Mesoporous Carbon as pH‐Universal Electrocatalyst for Oxygen Reduction Reaction. Adv Funct Mater. 2017;27(14).

[22] Mo Z, Liao S, Zheng Y, Fu Z. Preparation of nitrogen-doped carbon nanotube arrays and their catalysis towards cathodic oxygen reduction in acidic and alkaline media. Carbon. 2012;50(7):2620-7.

[23] Zhang C, Zhang G, Li H, Chang Y, Chang Z, Liu J, et al. Interfacial dehalogenation-enabled hollow N-doped carbon network as bifunctional catalysts for rechargeable Zn-air battery. Electrochim Acta. 2017;247:1044-51.

[24] Liu Q, Wang Y, Dai L, Yao J. Scalable fabrication of nanoporous carbon fiber films as bifunctional catalytic electrodes for flexible Zn-air batteries. Adv Mater. 2016;28(15):3000-6.

[25] Wang S, Qin J, Meng T, Cao M. Metal–organic framework-induced construction of actiniae-like carbon nanotube assembly as advanced multifunctional electrocatalysts for overall water splitting and Zn-air batteries. Nano Energy. 2017;39:626-38.

[26] Pei Z, Li H, Huang Y, Xue Q, Huang Y, Zhu M, et al. Texturing in situ: N, S-enriched hierarchically porous carbon as a highly active reversible oxygen electrocatalyst. Energy Environ Sci. 2017;10(3):742-9.

[27] Shinde SS, Lee C-H, Sami A, Kim D-H, Lee S-U, Lee J-H. Scalable 3-D carbon nitride sponge as an efficient metal-free bifunctional oxygen electrocatalyst for rechargeable Zn-air batteries. ACS nano. 2016;11(1):347-57.

[28] Jiang H, Wang Y, Hao J, Liu Y, Li W, Li J. N and P co-functionalized three-dimensional porous carbon networks as efficient metal-free electrocatalysts for oxygen reduction reaction. Carbon. 2017;122:64-73.

[29] Wu H, Geng J, Ge H, Guo Z, Wang Y, Zheng G. Egg‐Derived Mesoporous Carbon Microspheres as Bifunctional Oxygen Evolution and Oxygen Reduction Electrocatalysts. Advanced Energy Materials. 2016;6(20).

[30] Zhang J, Zhao Z, Xia Z, Dai L. A metal-free bifunctional electrocatalyst for oxygen reduction and oxygen evolution reactions. Nature Nanotech. 2015;10(5):444-52.

[31] Zhang J, Qu L, Shi G, Liu J, Chen J, Dai L. N,P-Codoped Carbon networks as efficient metal-free bifunctional catalysts for oxygen reduction and hydrogen evolution reactions. Angew Chem. 2016;128(6):2270-4.

[32] Zehtab Yazdi A, Roberts EPL, Sundararaj U. Nitrogen/sulfur co-doped helical graphene nanoribbons for efficient oxygen reduction in alkaline and acidic electrolytes. Carbon. 2016;100:99-108.

[33] Hu C, Dai L. Multifunctional Carbon‐Based Metal‐Free Electrocatalysts for Simultaneous Oxygen Reduction, Oxygen Evolution, and Hydrogen Evolution. Adv Mater. 2016.

[34] Zhang X, Liu R, Zang Y, Liu G, Wang G, Zhang Y, et al. Co/CoO nanoparticles immobilized on Co-N-doped carbon as trifunctional electrocatalysts for oxygen reduction, oxygen evolution and hydrogen evolution reactions. Chem Commun. 2016;52(35):5946-9.

[35] Yin J, Li Y, Lv F, Fan Q, Zhao Y-Q, Zhang Q, et al. NiO/CoN porous nanowires as efficient bifunctional catalysts for Zn-air batteries. ACS Nano. 2017;11(2):2275-83.

[36] Su C-Y, Cheng H, Li W, Liu Z-Q, Li N, Hou Z, et al. Atomic Modulation of FeCo–Nitrogen–Carbon Bifunctional Oxygen Electrodes for Rechargeable and Flexible All-Solid-State Zinc–Air Battery. Advanced Energy Materials. 2017;7(13):1602420-n/a.
[37] Wu X, Han X, Ma X, Zhang W, Deng Y, Zhong C, et al. Morphology-Controllable Synthesis of Zn–Co-Mixed Sulfide Nanostructures on Carbon Fiber Paper Toward Efficient Rechargeable Zinc–Air Batteries and Water Electrolysis. ACS Appl Mater Interfaces. 2017;9(14):12574-83.
[38] Jia Y, Zhang L, Du A, Gao G, Chen J, Yan X, et al. Defect graphene as a trifunctional catalyst for electrochemical reactions. Adv Mater. 2016;28(43):9532-8.
[39] Tian GL, Zhao MQ, Yu D, Kong XY, Huang JQ, Zhang Q, et al. Nitrogen‐Doped Graphene/Carbon Nanotube Hybrids: In Situ Formation on Bifunctional Catalysts and Their Superior Electrocatalytic Activity for Oxygen Evolution/Reduction Reaction. Small. 2014;10(11):2251-9.
[40] Peng Z, Yang S, Jia D, Da P, He P, Al-Enizi AM, et al. Homologous metal-free electrocatalysts grown on three-dimensional carbon networks for overall water splitting in acidic and alkaline media. J Mater Chem A. 2016;4(33):12878-83.
[41] Lai J, Li S, Wu F, Saqib M, Luque R, Xu G. Unprecedented metal-free 3D porous carbonaceous electrodes for full water splitting. Energy Environ Sci. 2016;9(4):1210-4.
[42] Zhang J, Dai L. Nitrogen, Phosphorus, and Fluorine Tri-doped Graphene as a Multifunctional Catalyst for Self-Powered Electrochemical Water Splitting. Angew Chem. 2016;128(42):13490-4.
[43] Fu G, Cui Z, Chen Y, Li Y, Tang Y, Goodenough JB. Ni_3Fe‐N Doped Carbon Sheets as a Bifunctional Electrocatalyst for Air Cathodes. Advanced Energy Materials. 2016.
[44] Liu T, Guo Y, Yan Y, Wang F, Deng C, Rooney D, et al. CoO nanoparticles embedded in three-dimensional nitrogen/sulfur co-doped carbon nanofiber networks as a bifunctional catalyst for oxygen reduction/evolution reactions. Carbon. 2016;106:84-92.
[45] Li X, Jiang Q, Dou S, Deng L, Huo J, Wang S. ZIF-67-derived Co-NC@CoP-NC nanopolyhedra as an efficient bifunctional oxygen electrocatalyst. J Mater Chem A. 2016;4(41):15836-40.
[46] Liu X, Zang J, Chen L, Chen L, Chen X, Wu P, et al. A microwave-assisted synthesis of CoO@Co core-shell structures coupled with N-doped reduced graphene oxide used as a superior multi-functional electrocatalyst for hydrogen evolution, oxygen reduction and oxygen evolution reactions. J Mater Chem A. 2017;5(12):5865-72.
[47] Liu X, Zhang M, Yu D, Li T, Wan M, Zhu H, et al. Functional materials from nature: honeycomb-like carbon nanosheets derived from silk cocoon as excellent electrocatalysts for hydrogen evolution reaction. Electrochim Acta. 2016;215:223-30.
[48] Sathe BR, Zou X, Asefa T. Metal-free B-doped graphene with efficient electrocatalytic activity for hydrogen evolution reaction. Catal Sci Technol. 2014;4(7):2023-30.
[49] Shinde SS, Sami A, Lee J-H. Electrocatalytic hydrogen evolution using graphitic carbon nitride coupled with nanoporous graphene co-doped by S and Se. J Mater Chem A. 2015;3(24):12810-9.